Atmospheric
Chemistry
and Physics

# Hemispheric differences in ozone across the stratosphere–troposphere exchange region

Rodrigo J. Seguel[1,2], Charlie Opazo[1,2], Yann Cohen[3], Owen R. Cooper[4], Laura Gallardo[1,2],
Björn-Martin Sinnhuber[5], Florian Obersteiner[5], Andreas Zahn[5], Peter Hoor[6], Susanne Rohs[7], and
Andreas Marsing[8]

[1]Center for Climate and Resilience Research CR2, Santiago, Chile
[2]Department of Geophysics, Faculty of Physical and Mathematical Sciences,
University of Chile, Santiago, Chile
[3]Institut Pierre-Simon Laplace (IPSL), Sorbonne Université/CNRS, Paris, France
[4]NOAA Chemical Sciences Laboratory, Boulder, CO, USA
[5]Karlsruhe Institute of Technology, Institute of Meteorology and Climate Research (IMK), Karlsruhe, Germany
[6]Institute for Atmospheric Physics, Johannes Gutenberg University, Mainz, Germany
[7]Institute of Energy and Climate Systems 3 – Troposphere (ICE-3), Forschungszentrum Jülich, Jülich, Germany
[8]Institute of Atmospheric Physics, German Aerospace Center (DLR), Oberpfaffenhofen, Germany

**Correspondence:** Rodrigo J. Seguel (rodrigoseguel@uchile.cl)

**Abstract.** Ozone changes in the upper troposphere–lower stratosphere (UTLS) resulting from dynamical and chemical processes strongly affect the atmosphere's radiative forcing. This study analyzed intra- and inter-hemispheric ozone differences in the UTLS within the 45–60° latitude band, distinguishing between years disrupted by sudden stratospheric warming (SSW) events from 2002 to 2022. We utilized measurements from IAGOS commercial aircraft (45–60° N), long-term ozonesonde records (45–60° S) and unique in situ measurements from the high altitude and long range (HALO) research aircraft deployed over the southernmost region of South America (45–60° S) in September–November 2019 as a part of the Southern Hemisphere Transport, Dynamics, and Chemistry (SouthTRAC) research campaign. The mission period enabled us to examine the impact of two Southern Hemisphere (SH) SSW events that developed during 2002 and 2019. To enhance the spatial coverage, we incorporated Copernicus Atmosphere Monitoring Service reanalysis data. Stratospheric air origin was assigned using relative humidity ($<20\%$) and carbon monoxide ($<50\,\mathrm{nmol\,mol^{-1}}$) thresholds. Our results show that air masses of stratospheric origin had higher ozone abundances in the Northern Hemisphere (NH) UTLS than in the SH (between 300–200 hPa and 45–60° latitude): in high ozone depletion years in the stratospheric vortex, the SH ozone median ($184\,\mathrm{nmol\,mol^{-1}}$) was only 54 % of that in the NH ($341\,\mathrm{nmol\,mol^{-1}}$), while in low depletion years, SH ozone median ($214\,\mathrm{nmol\,mol^{-1}}$) reached 57 % of the NH values ($371\,\mathrm{nmol\,mol^{-1}}$). Notably, the SSW events (2002 and 2019) increased SH UTLS ozone by 24 % ($43\,\mathrm{nmol\,mol^{-1}}$) compared to high depletion years, while in the NH, the increase was 9 % ($31\,\mathrm{nmol\,mol^{-1}}$).

# 1 Introduction

Ozone ($O_3$) has generated an effective radiative forcing (ERF) of $+0.47$ [0.24 to 0.71] W m$^{-2}$ over the industrial era, from 1750 to 2019. The ERF for ozone represents 17 % of the total anthropogenic ERF change, estimated at $+2.72$ [1.96 to 3.48] W m$^{-2}$ (Forster et al., 2021). The ozone abundance in the troposphere is related to the atmosphere's oxidizing capacity and is closely associated with methane abundance, the second-strongest greenhouse gas, due to hydroxyl radical ($\cdot$OH) reactions (Saunois et al., 2020). At ground level, short-term exposure to ozone impairs human lung function and contributes to the development of asthma symptoms in susceptible people (McConnell et al., 2002; Zheng et al., 2021). The total global mortality due to long-term ozone exposure has been estimated at 365 000 [175 000 to 564 000] deaths in 2019 (Health Effects Institute, 2020).

The tropospheric ozone budget is controlled by chemical production and loss, dry deposition, and stratosphere–troposphere exchange (STE) (Archibald et al., 2020). Oxidation of volatile organic compounds initiated by hydroxyl radicals leads to tropospheric ozone formation. During this process, hydroperoxyl ($HO_2$) and alkyl peroxy ($RO_2$) radicals reactions with nitric oxide (NO) yield nitrogen dioxide ($NO_2$), which photolyzes to produce ozone (Monks et al., 2015). In the troposphere, the chemical loss results mainly from ozone photolysis ($\lambda \leq 320$ nm) and ozone reaction with hydroxyl and hydroperoxyl radicals (Atkinson, 2000). An important ozone sink is dry deposition at the surface (Clifton et al., 2020).

The STE, estimated at $284 \pm 193$ Tg $O_3$ yr$^{-1}$ (Griffiths et al., 2021; Szopa et al., 2021), is comparable with the net chemical ozone production in the troposphere. STE involves several mechanisms, including tropopause folds within mid-latitude cyclones, cutoff-low decay and gravity wave breaking (Archibald et al., 2020; Cooper et al., 2004; Stohl et al., 2003). STE shows strong geographical asymmetry and seasonal cycles. STE dominates in the extratropics, with hotspots in the mountain regions of North and South America, over the Tibetan Plateau and in the storm tracks over the North Atlantic Ocean and North Pacific Ocean, which are more intense in winter and early spring in both hemispheres (Škerlak et al., 2014).

The poleward expansion of the Southern Hemisphere (SH) Hadley circulation has also been proposed as a mechanism able to enhance downward transport of ozone from the stratosphere to the troposphere at higher latitudes (Lu et al., 2019). The STE's contribution to the tropospheric ozone budget is expected to increase due to declining levels of ozone-depleting substances and the Brewer–Dobson circulation acceleration, especially in the lower stratosphere, caused by increasing greenhouse gas emissions (Butchart, 2014). In contrast, simulations based on climate models do not show Brewer–Dobson circulation acceleration in the mid-stratosphere of the mid-latitude Northern Hemisphere (NH)

since the late 1980s due to declining ozone-depleting substances and the timing of volcanic eruptions (Garfinkel et al., 2017).

Ozone changes in the upper troposphere–lower stratosphere (UTLS) strongly impact the radiative forcing of the atmosphere (Riese et al., 2012; Skeie et al., 2020). Therefore, in situ measurements in the UTLS, characterized by bidirectional trace gas exchange (Gettelman et al., 2011), are crucial to reducing the uncertainty of chemistry climate models and validating satellite retrievals (Bourgeois et al., 2020). Unfortunately, in the SH, measurements from IAGOS (In-service Aircraft for a Global Observing System: Petzold et al., 2015) commercial aircraft rarely extend beyond 35° S, and only a few aircraft-based research missions have characterized UTLS chemical composition in this area. The HALO (High Altitude and LOng range) aircraft measured dry air masses descending from the stratosphere down to an altitude of 7 km a.s.l. over the Antarctic in September 2012 (Rolf et al., 2015). Also, flights over the South Atlantic and South Pacific Oceans conducted by the Atmospheric Tomography mission measured a higher frequency of stratospheric intrusions during spring (Bourgeois et al., 2020). In addition, valuable long-term vertical ozone profiles have been obtained through ozonesonde launches at remote sites in higher latitudes of the SH, such as the Ushuaia (Argentina), Lauder (New Zealand) and Macquarie Island (Australia) stations, since 2008, 1986 and 1994, respectively (Zeng et al., 2024; Van Malderen et al., 2025).

In this context, the research project Southern Hemisphere Transport, Dynamics and Chemistry (SouthTRAC) was designed to comprehensively study the dynamical and chemical processes in the SH UTLS region using the HALO instrumented aircraft during the late winter and spring seasons (September–November) of 2019 (Rapp et al., 2021). SouthTRAC coincided with a polar stratospheric sudden warming (SSW) event that occurred in September 2019 (Rao et al., 2020; Rapp et al., 2021). SSW in the SH is a phenomenon that is unusual compared with the higher frequency of SSW events in the NH, with approximately one event per decade in the SH versus six in the NH (Dunn et al., 2020; Charlton and Polvani, 2007). SSW is caused by wave events that can decelerate the westerly polar night jet and warm the polar stratosphere by descending motion, resulting in reduced heterogeneous active chlorine formation onto polar stratospheric clouds and less catalytic ozone depletion (Scambos and Stammerjohn, 2020). Accordingly, the annual mean total ozone reported in 2019 was 65 DU higher than the long-term average, at 60–90° S (Dunn et al., 2020). The mission also coincided with intense Australian bushfires and biomass-burning events in central South America, which produced plumes detected by HALO in the UTLS (Kloss et al., 2021; Johansson et al., 2022).

Given the multiple dynamical and chemical processes that influence ozone in the UTLS (Millán et al., 2024; Bourgeois et al., 2020; Neu et al., 2014; Riese et al., 2012) and the

interhemispheric differences in processes such as the magnitude of the stratospheric ozone depletion and frequency of SSW events, this study investigates hemispheric differences in UTLS ozone in air masses of stratospheric origin, with focus on mid-latitudes, where STE plays a dominant role in determining ozone levels. We also leverage the increased ozone abundance under low-depletion conditions derived from SSW events to determine the intrahemispheric UTLS ozone differences. Through this comparative analysis, we aim to quantify the influence of two processes, i.e., stratospheric ozone depletion and SSW, on the ozone UTLS, where this species is an important radiative forcer. Our analysis utilized stratospheric and tropospheric chemical tracers measured during the SouthTRAC mission, by IAGOS commercial aircraft and by ozonesondes. Spatial coverage was further enhanced using the Copernicus Atmosphere Monitoring Service reanalysis (CAMSRA), which we compared against in situ measurements. Furthermore, by characterizing ozone and chemical species exchange in the UTLS, we identified a valuable dataset for evaluating the models that simulate ozone transport from the stratosphere to the troposphere in both hemispheres.

## 2 Data

The UTLS ozone measurements used in this study are available from (research and commercial) aircraft and ozonesondes. These in situ measurements were complemented with vertical ozone profiles obtained from chemical reanalysis. To determine the stratospheric or tropospheric origin of the ozone data, we used water vapor (or humidity) measurements from the aircraft and radiosondes coupled to the ozonesondes and from the chemical reanalysis in addition to carbon monoxide (CO), nitric acid ($HNO_3$) and hydrogen chloride (HCl) measurements from some of the aircraft data. In the next sections, we provide more details on these datasets.

### 2.1 SouthTRAC data

The SouthTRAC mission was conducted mainly over the southernmost region of South America within the latitudinal and meridional band 45–60° S and 55–85° W, respectively (Fig. 1). The mission had two stages: 9 September–6 October 2019 and 6–15 November 2019, totaling 16 flights, coinciding with the maximum ozone depletion in Antarctica. During this mission, the HALO aircraft was equipped with 13 instruments for sampling the physical and chemical properties of the atmosphere. This research focuses on the measurements of ozone, carbon monoxide, water vapor, nitric acid and hydrogen chloride. The number of measurements of each species is presented in Table 1.

In situ ozone was measured by the Fast AIRborne Ozone (FAIRO) monitor, provided by the Karlsruhe Institute of Technology, which combines two measurement principles: UV ozone absorption at 255 nm and dry chemiluminescence

from the reaction of ozone with an organic dye (coumarin) at 500 nm (Ermel et al., 2013). In this dual configuration, the UV photometer calibrated the chemiluminescence response. We utilized ozone records measured by chemiluminescence due to their higher sampling frequency (5 Hz) compared with UV photometry (0.25 Hz). Typical one standard deviation ($1\sigma$) measurement precision is 0.08 nmol mol$^{-1}$ for the UV spectrometer measuring at 0.25 Hz and $\sim 0.05$ nmol mol$^{-1}$ for the chemiluminescence detector measuring at 5 Hz, 1 bar and 5 nmol mol$^{-1}$ absolute mixing ratio (Zahn et al., 2012). The estimated uncertainty for UV photometer measurements was 2 % and for the combined techniques (UV and chemiluminescence) was 2.5 %.

The University of Mainz Airborne Quantum Cascade Laser Spectrometer measured in situ carbon monoxide. This instrument is based on direct absorption in the near-infrared through a continuous-wave quantum cascade laser (Müller et al., 2015). The instrument had a typical carbon monoxide precision of 0.68 nmol mol$^{-1}$ ($2\sigma$), an accuracy of 1.2 nmol mol$^{-1}$ and a total uncertainty of 1.4 nmol mol$^{-1}$.

Static pressure and static temperature were measured by the Basic HALO Measurement and Sensor System (BAHAMAS) with estimated accuracies of 0.3 hPa and 0.5 K, respectively (Giez et al., 2017; Kaufmann et al., 2018). BAHAMAS also measured water vapor at the absorption line of 1.37 µm using the Sophisticated Hygrometer for Atmospheric ResearCh (SHARC), a tunable diode laser hygrometer. The limit of detection of the SHARC measurement achieved during SouthTRAC campaign was 2 µmol mol$^{-1}$ with an absolute uncertainty of $\pm 1$ µmol mol$^{-1}$ (Kaufmann et al., 2018).

Nitric acid and hydrogen chloride were measured using the Airborne Chemical Ionization Mass Spectrometer. In this system, the ion source generates reagent ions ($SF_5^-$) that selectively react with $HNO_3$ and HCl to form $HFNO_3^-$ and $HFCl^-$, respectively. A fast quadrupole mass spectrometer then separates the ion products based on their mass-to-charge ratio. Typical accuracy, precision ($1\sigma$) and limit of detection are 16 %, 20 % and 20 pmol mol$^{-1}$ for $HNO_3$ and 12 %, 16 % and 15 pmol mol$^{-1}$ for HCl, respectively (Jurkat et al., 2016).

### 2.2 Ozonesonde data

Ozone profiles from ozonesondes launched at Ushuaia, Argentina (54.85° S, 68.31° W), and Macquarie Island, Australia (54.50° S, 158.95° E), were obtained from the World Ozone and Ultraviolet Radiation Data Centre (WOUDC; https://woudc.org/, last access: 31 July 2024), while ozone profiles from Lauder, New Zealand (45.04° S, 169.68° E) were obtained from the Tropospheric Ozone Assessment Report – Phase II (TOAR-II) Focus Working Group HEGIFTOM (Harmonization and Evaluation of Ground-Based Instruments for Free Tropospheric Ozone Measurements). These data were included in our research in order to compare SouthTRAC measurements to historical data.
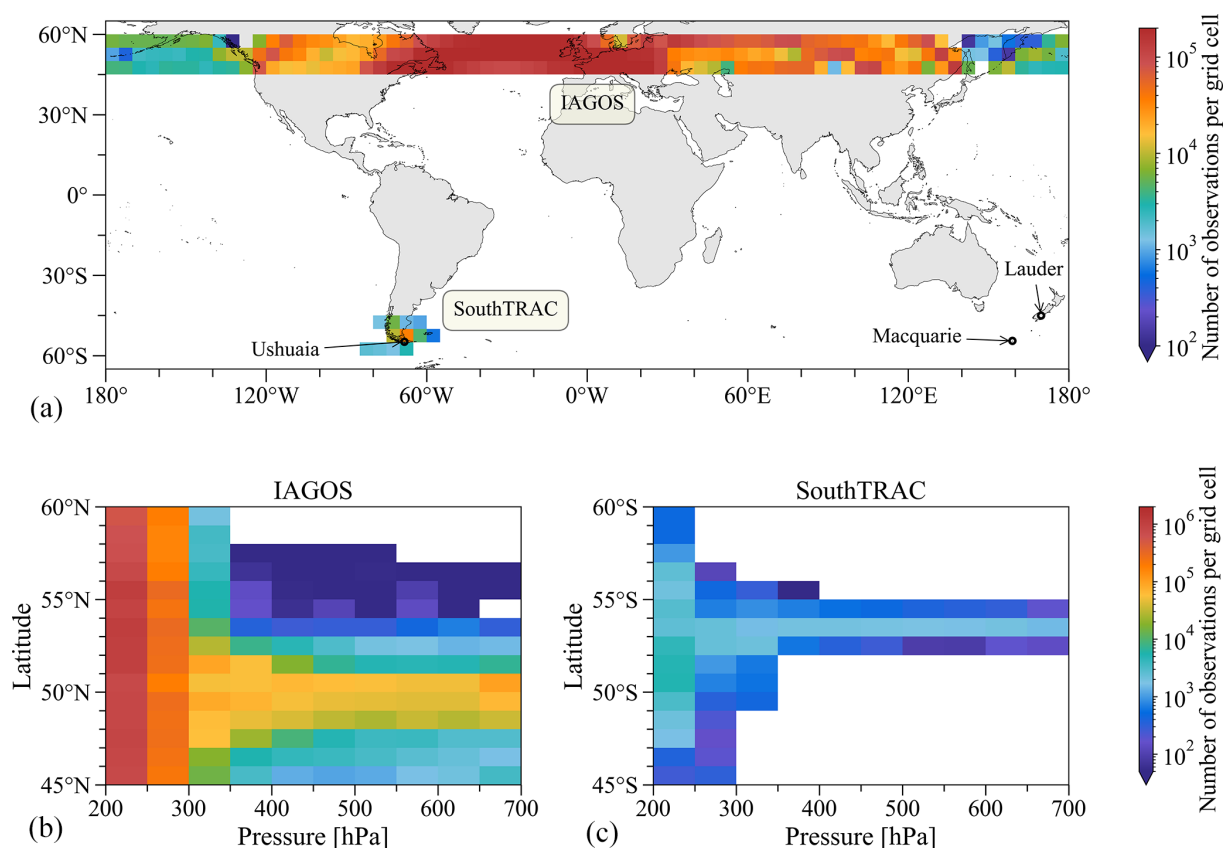
**Figure 1.** Routes position frequency obtained from aircraft GPSs. All panels show only SouthTRAC and IAGOS data within the same latitudinal band 45–60° in the SH and NH. SouthTRAC shows data from 4 September to 20 November 2019 and IAGOS between 4 March and 20 May from 2002 to 2022. The upper panel shows the number of GPS observations by grid cell (5° × 5°) between 700 and 200 hPa. Panels **(b)** and **(c)** show the number of GPS observations in every grid cell (1° × 50 hPa) between 700 and 200 hPa for IAGOS **(b)** and SouthTRAC **(c)**. **(a)** also indicates the location of the ozonesonde sites of Ushuaia, Lauder and Macquarie Island.

These ozonesondes were coupled with radiosondes, which measured pressure, temperature, RH, wind speed and wind direction. Table 1 shows the available periods utilized in this study and the number of validated flights from each site. The ozonesondes were linearly interpolated to an altitude grid with intervals of 50 m (Ohyama et al., 2018).

During 2002–2022, several radiosonde models were utilized interchangeably (e.g., Lauder). The Vaisala RS92 and its replacement RS41 sensor are among the most frequently used models. Regarding RH, the latter performs better than the older version, particularly under cloudy conditions (Jensen et al., 2016). Overall, both sensors have an uncertainty of 5 % and show a consistent difference of about 1 %–2 %, with the RH of the RS41 almost always greater than RS92 (Jensen et al., 2016).

## 2.3 IAGOS data

The IAGOS research infrastructure provides in situ measurements of chemical species on board several commercial aircraft. IAGOS is a continuation of the former observation systems MOZAIC (Measurement of Ozone and Water Vapor by Airbus In-Service Aircraft: Marenco et al., 1998) and also includes the CARIBIC measurement system (Civil Aircraft for the Regular Investigation of the Atmosphere Based on an Instrument Container: Brenninkmeijer et al., 1999, 2007; Stratmann et al., 2016), now called IAGOS-CORE and IAGOS-CARIBIC.

The MOZAIC observations started in August 1994 for ozone and water vapor on board five equipped aircraft, whereas the carbon monoxide measurements started in December 2001. The CARIBIC observations started in 1997 for a wide range of chemical species, including ozone, water vapor and carbon monoxide, on a single aircraft.

IAGOS-CORE provides ozone (and carbon monoxide) data using an ultraviolet (infrared) absorption spectrometer, with an accuracy, precision and time response of $2 \, \text{nmol mol}^{-1}$, 2 % and 4 s ($5 \, \text{nmol mol}^{-1}$, 5 %, 30 s), respectively (Nedelec et al., 2003; Nédélec et al., 2015; Thouret et al., 1998). Water vapor is measured with a capacitive hygrometer, characterized by an accuracy of 5 % in RH with respect to liquid water (RHL), or 6 % RHL in the vicinity of

**Table 1.** Summary of data used. The columns detail dataset sources, spatial coverage, temporal periods, the number of flights in the period and the number of measurements for each variable (in ozonesondes is the number of interpolated measurements) between 200–300 hPa.

| Data source | Hemisphere or site (lat., lon.) | Periods | No. flights or valid launches | Variable (no. measurements) |
|---|---|---|---|---|
| SouthTRAC | SH (45–60° S, 55–85° W) | 4 September– 20 November 2019 | 16 | Pressure: : 42 848 $O_3$: 38 612 CO: 26 279 $H_2O$: 42 848 RH: 42 848 |
| WOUDC | Ushuaia (54.85° S, 68.31° W), | 2008–2022 | 141 | Pressure: 7119 $O_3$: 7119 RH: 7119 |
| | Lauder (45.04° S, 169.68° E), | 2002–2022 | 232 | Pressure: 12 113 $O_3$: 12 113 RH: 12 075 |
| | Macquarie (54.50° S, 158.95° E) | 2002–2022 | 203 | Pressure: 10 611 $O_3$: 10 611 RH: 10 611 |
| IAGOS | NH (45–60° N) | 2002–2022 | 6315 | Pressure: 16 295 947 $O_3$: 11 393 231 CO: 11 148 354 $H_2O$: 14 096 134 RH: 14 773 909 |

the thermal tropopause at midlatitudes, and a time response of 5–300 s (Helten et al., 1998; Neis et al., 2015; Rolf et al., 2024; Smit et al., 2014).

IAGOS-CARIBIC uses an identical instrument to measure ozone as described for HALO (see Sect. 2.2). Carbon monoxide data are measured by a commercial resonance fluorescence UV instrument modified for use onboard commercial aircraft. Its accuracy, precision and time response are, respectively, less than 2 nmol mol$^{-1}$, 1–2 nmol mol$^{-1}$, and less than 2 s (Scharffe et al., 2012). Water vapor measurements are performed with a photoacoustic laser spectrometer and a frost-point hygrometer, with an accuracy of less than 4 % or 0.3 µmol mol$^{-1}$ for the mixing ratio. The time response varies between 5 and 30 s for humid (>100 ppm) and dry air masses (<10 ppm) respectively (Dyroff et al., 2015; Zahn et al., 2014).

## 2.4 CAMS & ERA5 reanalysis

We utilized vertical ozone profiles, temperature and specific humidity from the chemical reanalysis CAMSRA, which has 60 model levels from the surface to the top of the atmosphere, a horizontal resolution of 0.75° × 0.75° and a time resolution every 3 h (Inness et al., 2019). We also retrieved zonal wind at 60° N (60° S) and 10 hPa from ERA5 reanalysis (Hersbach et al., 2023). ERA5 has hourly resolution, 0.25° × 0.25° horizontal resolution and 37 pressure levels. We used post-

processed daily mean on pressure levels obtained from the Copernicus Climate Change Service Climate Data Store.

## 3 Method

In this section, we describe how we used the data available to analyze late winter mid-spring UTLS ozone differences at the mid-latitudes between both hemispheres. We first describe our study period and the used UTLS definition (Sect. 3.1), then we mention how we distinguish between high and low stratospheric ozone depletion years (Sect. 3.2) and show how we ascertain the stratospheric origin of the analyzed UTLS ozone mixing ratios (Sect. 3.3).

## 3.1 Study period & UTLS definition

In this study, we denominate the UTLS as the segment between 200 (∼ 12 km) and 300 (∼ 9 km) hPa, while the free troposphere is the segment between 700 to 300 hPa. We focus on the period between late winter and mid-spring in both hemispheres: 4 September–20 November (SH) and 4 March–20 May (NH). For comparison, IAGOS data from 2002 to 2022 were analyzed for the same latitudinal band and altitude range in the NH. Figure 1 shows the sampling density given by the aircraft's positional data to identify those regions of the atmosphere with more data availability. In addition, Fig. S1 in the Supplement depicts the highest num-

ber of GPS observations obtained between 300 and 200 hPa compared to the range of 700 to 300 hPa.

## 3.2  High and low ozone depletion years definition

We distinguished low ozone depletion years from high ozone depletion years according to the occurrence of SSW events. Therefore, we applied the definition proposed by Charlton and Polvani (2007) and used ERA5 data to detect major SSW, which is based on determining the reversal of the daily mean zonal-mean zonal winds from westerly to easterly at 60° N and 10 hPa from November to April. Table 2 shows the so-called central date (Charlton and Polvani, 2007), i.e., the first day on which the daily zonal-mean zonal wind at 10 hPa and 60° N changed from westerly to easterly between November and March. During the detection procedure, we required 20 consecutive days with westerly winds before identifying another event. We excluded cases with easterly zonal winds that did not return to westerly for at least 10 consecutive days before 30 April. In the SH, the shift from westerly to easterly is considered between July and October, and we excluded the cases when the wind did not return to westerly by 30 November.

In addition to the 2002 major SSW identified by the above metric, this research also considered the 2019 SH SSW as a low ozone depletion year. While the 2019 event did not reverse the zonal wind at 60° S and 10 hPa, the weakening of the stratospheric polar vortex was as strong as that of the 2002 event (Lim et al., 2021; Rao et al., 2020).

Additionally, given that the ozone-depleted air masses typically reach their minimum ozone content in October (March) of the Southern (Northern) Hemisphere, we split the flights into late winter–early spring and mid-spring, representing the latter, the period when depleted ozone air likely reaches the SouthTRAC study region (Table 2).

## 3.3  Stratospheric character determination

Stratospheric and tropospheric tracer scatterplots provide a magnitude of bidirectional exchange across the tropopause by the identification of stratospheric and tropospheric branches and mixed air regions according to their tracer abundances (Gettelman et al., 2011). Hence, in this study, our first analysis used tracer correlations to compare the Northern Hemisphere (IAGOS) and Southern Hemisphere (SouthTRAC) mid-latitudes, and between high and low ozone depletion years (NH).

We utilized several sensors with different accuracies to filter air masses by RH. Vaisala radiosonde sensors have a longer response time, and their vertical resolution highly depends on temperature; thus, radiosonde sensors are less accurate than SHARC, IAGOS-CORE and IAGOS-CARIBIC measurements. Therefore, we tested different relative humidity levels, from 50 % to 10 % (every 10 intervals), to effectively filter tropospheric moist mid-latitude air masses. We

estimated that a RH lower than 20 % is effective in excluding tropospheric air masses richer in water vapor and is sufficiently conservative, given the sensor accuracy. This threshold behaves similarly to the 50 nmol mol$^{-1}$ carbon monoxide filter (analyzed in more detail in Sect. 4.2).

CAMSRA profiles were also filtered using 20 % RH for the 45–60° N and 45–60° S zonal bands between 2003 and 2022 (Table 1). In this case, we calculated the relative humidity with respect to liquid water from temperature and specific humidity.

## 4  Results and discussion

In the following section, we used tracer correlations to characterize the tropospheric or stratospheric origin of the air masses in the UTLS and free troposphere of both hemispheres. In Sect. 4.2, we applied filters mainly based on the relative humidity to assign the stratospheric origin in the UTLS and then determine the inter- and intra-hemispheric ozone differences. Finally, in Sect. 4.3, we compare the results based on situ ozone measurements with CAMSRA outputs.

## 4.1  Tropospheric and stratospheric tracer correlations

Tracer-to-tracer scatterplots between stratospheric ozone tracer and tropospheric tracers, such as water vapor and carbon monoxide at two pressure intervals, are shown in Figs. 2 and 3. In general, we observed higher ozone values in the UTLS and free troposphere of the NH compared to the SH. The scatterplots show that ozone between 300–200 hPa in the SH rarely exceeds 400 nmol mol$^{-1}$. In contrast, in the NH, high ozone levels near 1200 nmol mol$^{-1}$ associated with low water vapor levels (i.e., drier air) are observed. The same pattern is observed between 700 and 300 hPa, with ozone levels in the NH being much higher than those observed in the SH (up to an excess of 200 nmol mol$^{-1}$). Figure 2 also shows a similar relationship between ozone and water vapor in low and high depletion years at both pressure intervals in the NH. In the following section, we clearly distinguish the ozone differences between the low and high depletion years.

Tracer-to-tracer scatterplots of ozone and carbon monoxide show that in the NH, carbon monoxide reaches higher levels ($\sim$ 300 nmol mol$^{-1}$) at both 300–200 and 700–300 hPa (Fig. 3). Notice that some carbon monoxide values are not included in the NH because they were not simultaneously measured with ozone. Again, carbon monoxide and ozone show a similar relationship in low and high depletion years in the NH. In contrast, in the SH, carbon monoxide rarely exceeds 100 nmol mol$^{-1}$ in both pressure intervals (300–200 and 700–300 hPa). An exception to this behavior was observed during the flight conducted on 12 November 2019 (mid-spring), which detected elevated levels of carbon monoxide ($>$200 nmol mol$^{-1}$), ozone ($>$100 nmol mol$^{-1}$) and water vapor ($>$100 µmol mol$^{-1}$) at pressures below 300 hPa.

**Table 2.** Study period considered for both hemispheres, subperiods and low ozone depletion years according to the SSW definition.

| Study period | Late winter–early spring (no. of flights or launches) | Mid-spring (no. flights or launches) | Low-depletion years (central date) |
|---|---|---|---|
| 4 March–20 May | 4–31 March (2142 IAGOS flights) | 1 April–20 May (4173 IAGOS flights) | 2002 (17 February), 2003 (18 January), 2004 (5 January), 2006 (21 January), 2007 (24 February), 2008 (22 February), 2009 (24 January), 2010 (24 March), 2013 (6 January), 2018 (12 February), 2019 (1 January) and 2021 (5 January) |
| 4 September–20 November | 4–30 September (10 SouthTRAC flights) (204 launches) | 1 October–20 November (6 SouthTRAC flights) (372 launches) | 2002 (25 September) and 2019* (15 September) |

* Central date determined when the zonal-mean zonal winds at 60° S and 10 hPa decrease to $\leq 20\,\mathrm{m\,s^{-1}}$ (Rao et al., 2020).
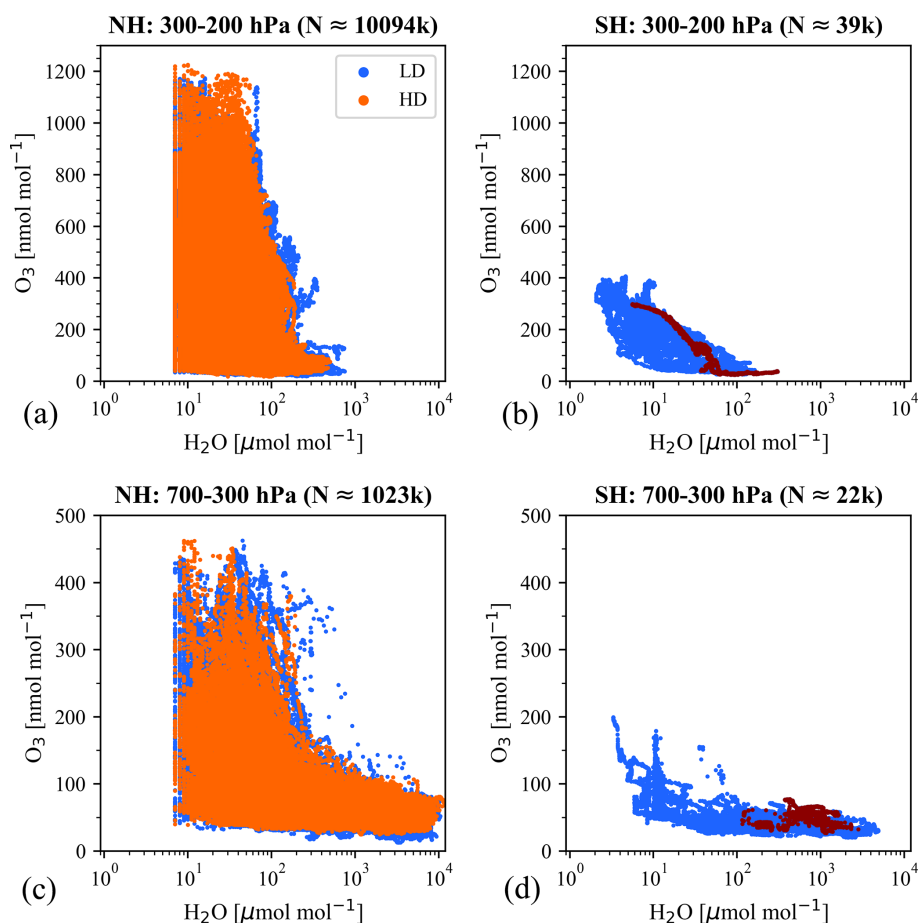


**Figure 2.** Scatter plots of ozone versus water vapor. **(a)**, **(c)** show scatter plots for the period between 4 March and 20 May from 2002 to 2022 for the NH between 300–200 and 700–300 hPa (IAGOS dataset described in Table 1). Panels **(b)** and **(d)** show the same for the SH between 4 September and 20 November 2019 (SouthTRAC data described in Table 1). Low and high depletion (LD and HD) years are in blue and orange colors, respectively. Above each plot, $N$ stands for the number of observations. In the SH, the flight conducted on 12 November 2019 is highlighted in dark red.
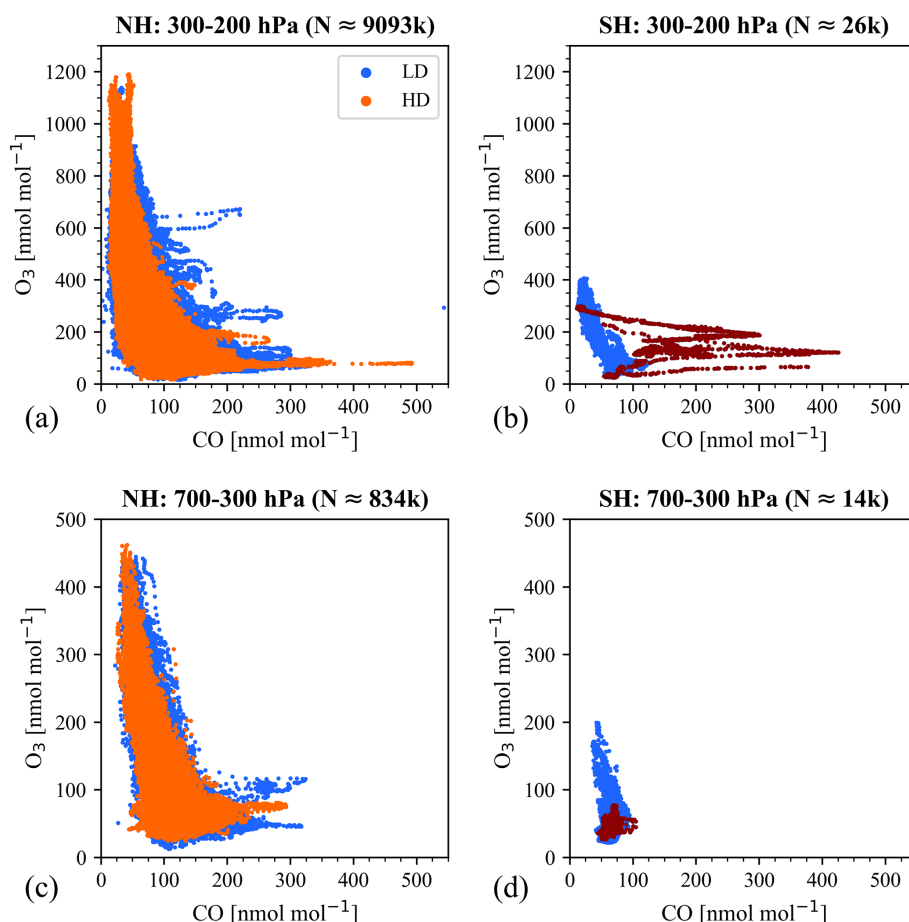
**Figure 3.** Scatter plots of ozone versus carbon monoxide. **(a)**, **(c)** show scatter plots for the period between 4 March and 20 May from 2002 to 2022 for the NH between 300–200 and 700–300 hPa (IAGOS dataset described in Table 1). **(b)**, **(d)** show the same for the SH between 4 September and 20 November 2019 (SouthTRAC campaign data described in Table 1). Low and high depletion (LD and HD) years are in blue and orange colors, respectively. Above each plot, $N$ stands for the number of observations. In the SH, the flight conducted on 12 November 2019 is highlighted in dark red.

These elevated levels were attributed to tropospheric plumes and may have been pyrogenic in origin, given the simultaneous bushfires in Australia that extended from September 2019 to March 2020 (Kloss et al., 2021). Ultimately, the impact of emissions from the Australian bushfires in the UTLS may be interpreted as feedback initiated early in August–September 2019, which derived from the deceleration of the polar vortex in the middle stratosphere.

In this regard, the abundance of nitric acid and hydrogen chloride are also useful in determining the plume's origin since these two species are stable in the stratosphere but more prone to removal in the troposphere. Tracer-to-tracer scatterplots of these species versus ozone and carbon monoxide (Fig. 4) show that nitric acid and hydrogen chloride were generally higher when ozone was higher and lower when carbon monoxide was higher. This anticorrelation between carbon monoxide and stratospheric tracers suggests that this plume predominantly originates from the troposphere. Nevertheless, we cannot entirely exclude the mixing processes

of stratospheric and tropospheric air masses, as shown by the fluctuations registered during the flight (Fig. 4).

Overall, in this section, we found that the NH does not show differences between high and low depletion years. Therefore, in the following section, we test different filters to isolate the air of stratospheric origin in the UTLS and thus investigate its ozone mixing ratios during high and low depletion years in both hemispheres. In this section we also showed that the NH has higher carbon monoxide levels than the SH and a threshold of $50\,\mathrm{nmol\,mol^{-1}}$ at 300–200 hPa seems to well represent the stratospheric branch in both hemispheres (Fig. 3). Accordingly, we utilized the carbon monoxide levels ($<50\,\mathrm{nmol\,mol^{-1}}$) in the following section to distinguish stratospheric air masses, even though our primary classification relies on the RH threshold.
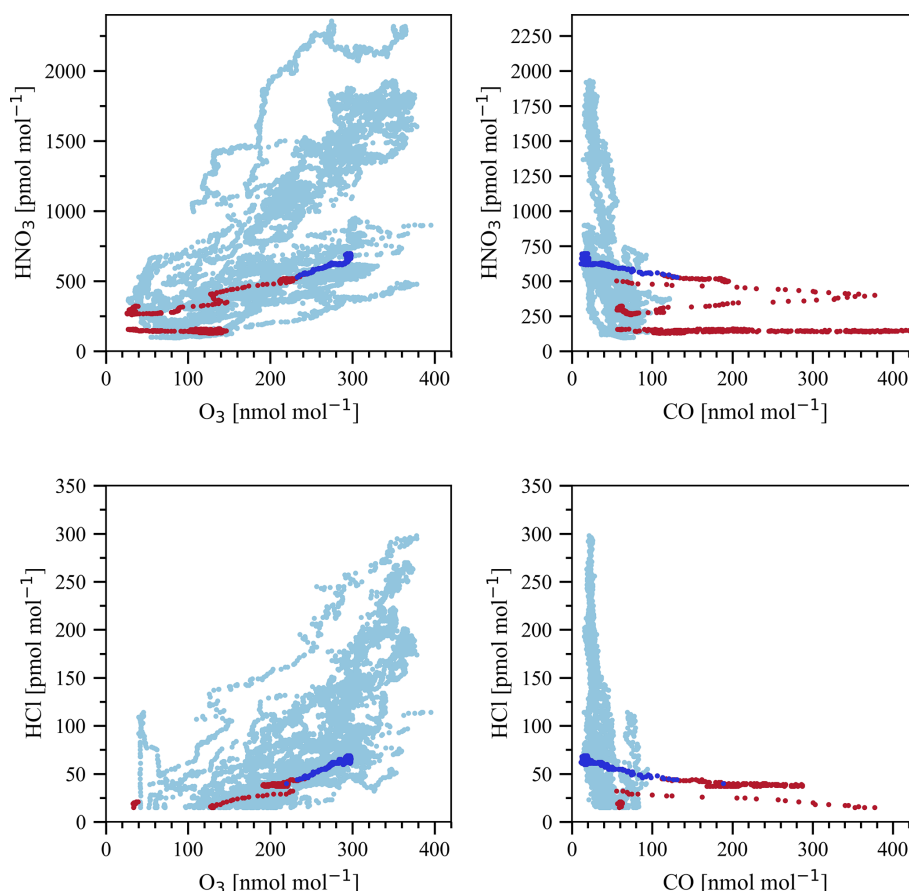
**Figure 4.** Scatter plots of nitric acid versus ozone, nitric acid versus carbon monoxide, hydrogen chloride versus ozone and hydrogen chloride versus carbon monoxide. These scatter plots are based exclusively on SouthTRAC data. Measurements obtained during the flight conducted on 12 November 2019 (ST25) are highlighted from the other flight measurements depending on their relative humidity in blue ($<20\%$) or in red ($>20\%$).

## 4.2 Inter and intrahemispheric ozone differences in the UTLS

As discussed earlier in the methodology, aircraft RH observations are more accurate than radiosondes. Therefore, we tested several RH filters on the air masses, aiming to minimize the impact of the reported error of the sensors within the UTLS and to minimize the inclusion of tropospheric air. The following discussion is based on a 20 % RH filter, while results for 30 % and 10 % RH are shown in the Supplement (Figs. S2 and S3). Figure 5 depicts ozone boxplots and the corresponding observation numbers (in the 10-base logarithm) by pressure bins. It is worth noting that the pressure bins between 300 and 280 hPa have less data, particularly those obtained from aircraft sampling (Fig. 5), which implies a lower representativity at the lowest altitude bins. The same observation applies to the 230–220 hPa bin during mid-spring in the SouthTRAC mission. In the appendix (Fig. A1), we also present the ozone boxplots without filters to visualize the aspect of the original data. The filter's applicability can be clearly verified for the subperiod late winter–early spring in the SH, where differences between high and low ozone depletion years can be noticed without any filter (Fig. A1). However, we can also note that the 20 % RH filter is very effective at removing the lowest ozone mixing ratios with tropospheric origin (or mixed air).

We observed higher ozone abundances in the NH for the entire period analyzed and for both subperiods, i.e., late winter–early spring and mid-spring compared with the SH (Fig. 5). We also noticed differences between high- and low-depletion years in both hemispheres. To provide a quantitative magnitude of these differences, we averaged the medians between 300 and 200 hPa (shown in Fig. 5) and then calculated the ozone difference (and standard deviation) between low- and high-depletion years. In the NH, ozone in low-depletion years increased by 9 % ($31 \pm 11$ nmol mol$^{-1}$) compared with high depletion years. The changes in the subperiods late winter–early spring and mid-spring were similar, with 8 % ($26 \pm 22$ nmol mol$^{-1}$) and 10 % ($36 \pm 12$ nmol mol$^{-1}$), respectively.
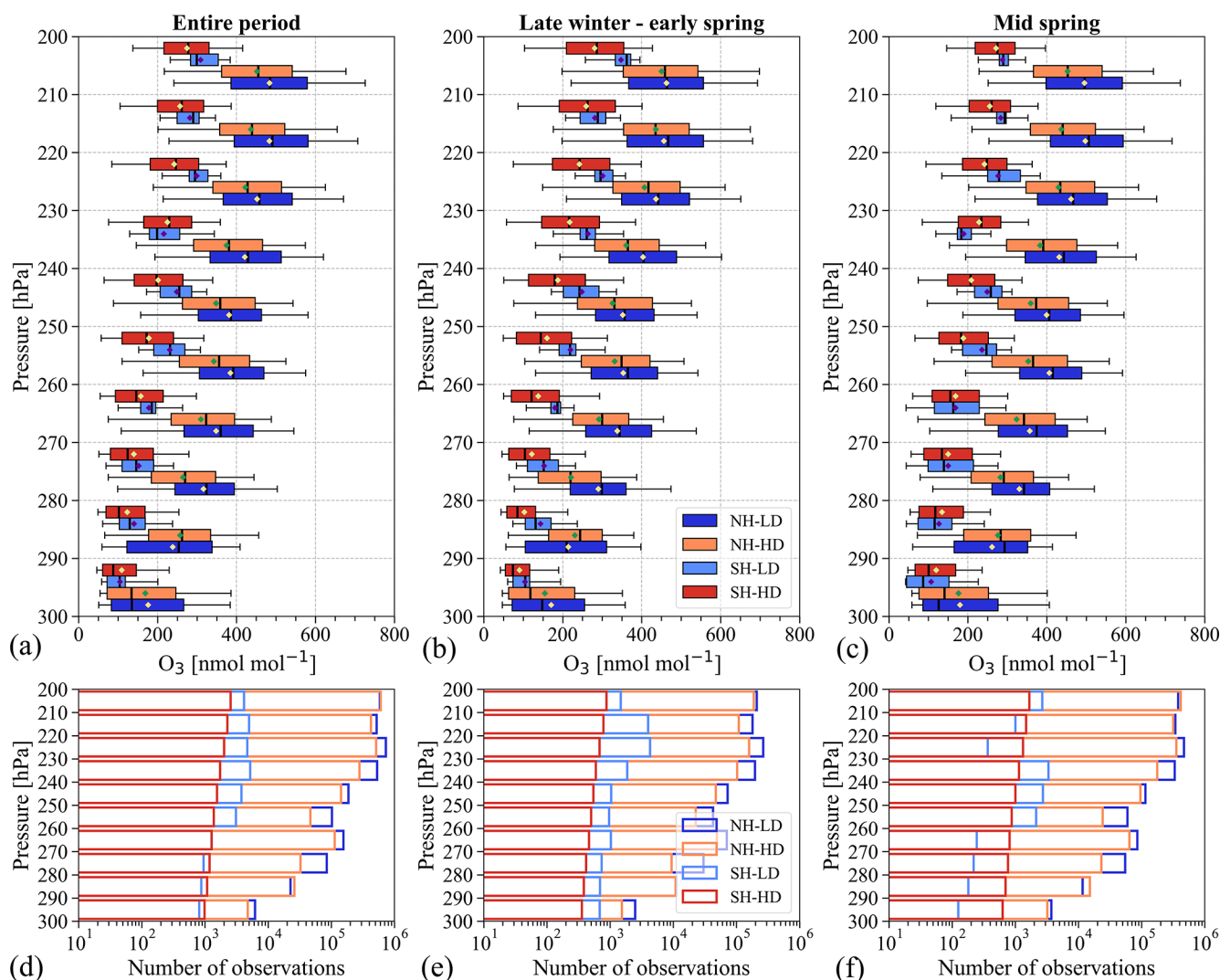
**Figure 5.** Ozone boxplot (nmol mol$^{-1}$) and associated sample sizes by pressure bins. The plots include ozone data with RH less than 20 % obtained from IAGOS, SouthTRAC and WOUDC (Table 1). In the upper panel, **(a)**, **(b)** and **(c)** show the entire period, late winter–early spring and mid-spring, respectively, for the Northern Hemisphere and Southern Hemisphere and high-depletion (HD) and low-depletion (LD) years. Boxplots indicate the median, the 25th and 75th percentiles. The diamonds in panels **(a)**, **(b)** and **(c)** indicate the mean values. The whiskers extend to the 5th and 95th percentiles. In panels **(d)**, **(e)** and **(f)**, the $x$ axis shows the observation numbers. The rest of the plot information is the same as described in panels **(a)**–**(c)**. High- and low-depletion years in SH included ozonesondes launched from Ushuaia, Lauder and Macquarie Island.

In the SH, the ozone difference between high- and low-depletion years was more intense in late winter–early spring, especially for pressures less than 270 hPa. Within 300–200 hPa, the difference between medians averaged $53 \pm 17$ nmol mol$^{-1}$, being on average 31 % greater relative to high depletion years (Fig. 5). The observed change in mid-spring was more variable. We attribute this behavior to the shorter time of flight in some pressure bins. On the other hand, the 2019 data are heavily influenced by the SouthTRAC sample size despite including three ozonesonde sites, as shown in Fig. B1, where the ozone boxplots are without SouthTRAC data. Interestingly, by excluding South-

TRAC data, the mid-spring period is consistently higher in low depletion years at all pressure bins and reproduced ozone's higher difference in late winter–early spring. Hence, considering only ozonesondes, the enhancement for mid-spring was 17 % ($33 \pm 10$ nmol mol$^{-1}$) and for the entire period (SouthTRAC combined with ozonesondes) it was 24 % ($43 \pm 13$ nmol mol$^{-1}$).

The higher ozone levels observed in the late winter–early spring during the 2002 and 2019 SH SSW (45–60° S), compared with high depletion years (2002–2022), clearly illustrate the impact of the early warming of the polar vortex in September 2019, which was even earlier than the Septem-
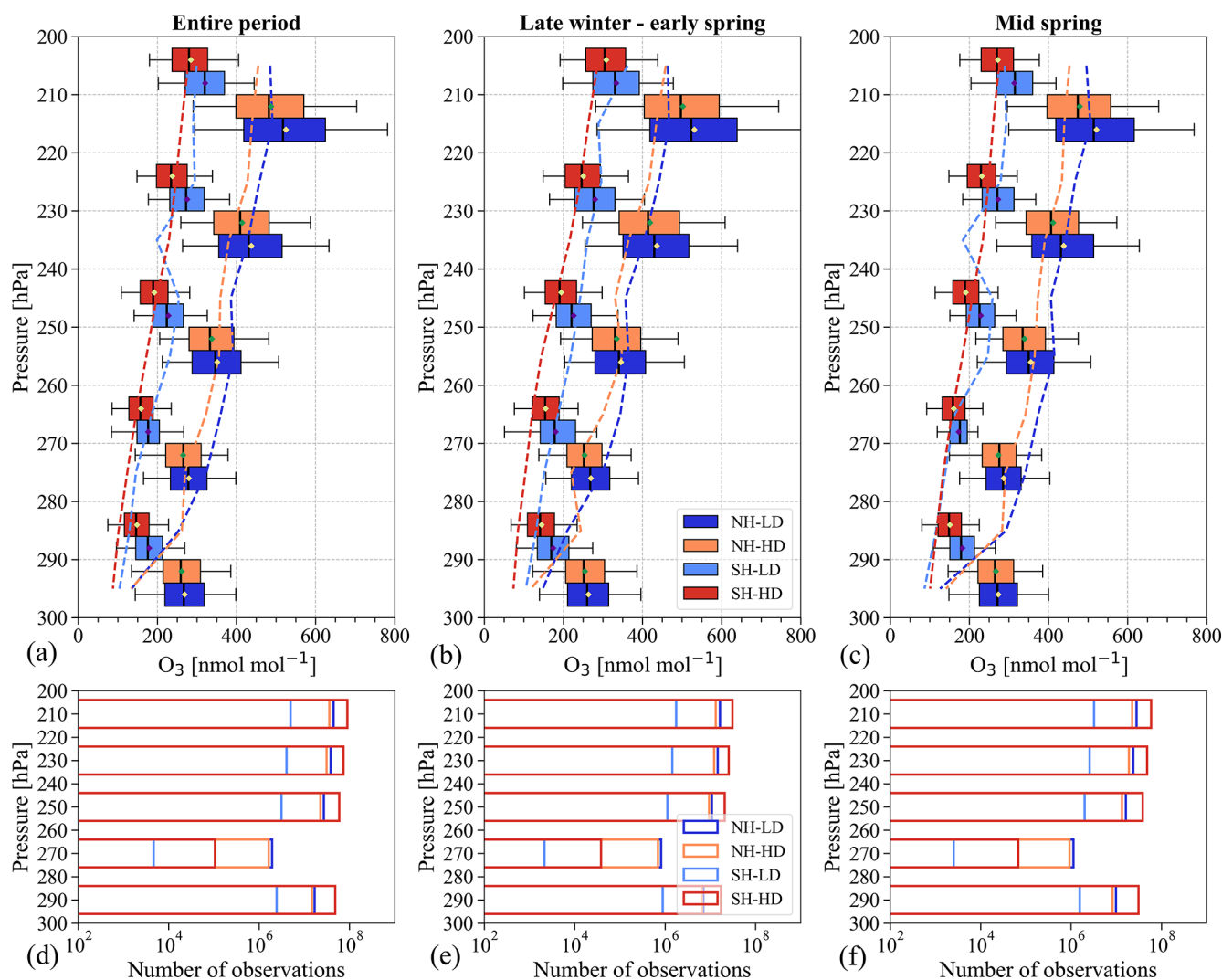
**Figure 6.** Ozone boxplot (nmol mol$^{-1}$) and associated sample sizes by pressure bins obtained from the CAMS reanalysis. The plots include ozone data with RH less than 20 %. The vertical dashed lines are the ozone medians obtained through in situ measurements previously shown in Fig. 5. In the upper panel, the **(a)**, **(b)** and **(c)** show the entire period, late winter–early spring and mid-spring, respectively, for the Northern Hemisphere and Southern Hemisphere and HD and LD years. Boxplots indicate the median and the 25th and 75th percentiles. The diamonds in panels **(a)**–**(c)** indicate the mean values. The whiskers extend to the 5th and 95th percentiles. In **(d)**–**(f)**, the $x$ axis shows the observation numbers. The rest of the plot information is the same as described in panel **(a)**–**(c)**.

ber 2002 warming (Scambos and Stammerjohn, 2020). In this region, Antarctic ozone depletion, more intense between 12 and 20 km, typically begins in August, accelerates in September, and reaches a minimum in October when ozone starts to recover. Therefore, the period of higher ozone destruction rate in September was entirely captured by the SouthTRAC mission.

Although the magnitude of the SSW event was not categorized as a major event, i.e., easterly winds did not reverse at 10 hPa at 60° S, it was strong enough to decrease the halogen-catalyzed ozone loss over the polar region and be detected in subpolar regions as shown in Fig. 5. Later, in mid-spring, the observed ozone changes were less intense. Nonetheless, it is

worth noting that even during this less ozone-depleted atypical scenario in 2019, the ozone abundance in the UTLS was not comparable to the higher levels observed in the NH, representing only 57 % of the NH ozone median.

The agreement between carbon monoxide and 20 % RH filters varies with pressure bins, with a better agreement at pressures less than 270 hPa and where more aircraft measurements were available. On average, between 270 and 200 hPa, the percentage ozone difference between both filters was 13 ± 16 % in low depletion years (NH), 15 ± 8 % in high depletion years (NH) and 5 ± 6 % in low depletion years (SH). In the SH, we have compared only the low-depletion years because carbon monoxide was measured only by the South-

TRAC mission. Thereby, Fig. C1 shows the ozone abundances by pressure bins after applying the carbon monoxide filter ($<50$ nmol mol$^{-1}$). Similarly to the 20 % RH filter, less ozone abundances were observed in the SH during low-depletion years compared with the NH, and a similar pattern can be observed for the ozone difference between high and low-depletion years in the NH.

## 4.3 Outputs comparison based on in situ measurement and reanalysis

So far, we have provided ozone mixing ratios (in drier air) for the entire longitudinal band without paying attention to spatial asymmetries previously reported in the literature (Škerlak et al., 2014). Therefore, the motivation of this section is to compare the in situ measurements of ozone, filtered by 20 % RH in the UTLS, with the values produced by the CAMS reanalysis over the entire longitudinal band within 45–60° latitude and for low and high depletion years indicated in Table 2, aiming to provide a spatially resolved perspective.

In Fig. 6, the ozone boxplot is displayed in five pressure bins, determined by the five vertical levels available for CAMSRA in 300–200 hPa. Figure 6 shows that the reanalysis reproduces the ozone interhemispheric differences, i.e., higher ozone in the NH and differences between high and low ozone depletion years. We also compared the pattern agreement between the ozone boxplots (CAMSRA) and in situ measurements. Figure 6 clearly illustrates the similarity between the ozone medians obtained from the CAMSRA and in situ measurements (SouthTRAC and ozonesondes) particularly in the period with the highest number of flights, i.e., late winter–early spring, for pressures lower than 270 hPa. The lower agreement between the ozone medians of CAMSRA and in situ measurements in the mid-spring period was determined by the lower flight frequency in this period, i.e., six flights during the mid-spring period versus ten in the late winter–early spring period (also discussed in Sect. 4.2). Regardless, we can observe the similarity of the ozone medians obtained from ozonesondes and the reanalysis for the entire period (less affected by the mid-September SouthTRAC data).

Figure 7 shows CAMS reanalysis across the entire NH and SH longitudinal band for high and low depletion years from 2003 to 2022. Consistently, the spatial distribution of ozone median (filtered by 20 % RH) in the UTLS obtained by CAMSRA reproduced the hemispheric differences discussed previously. Mean UTLS ozone during high and low ozone depletion years was 399 and 425 nmol mol$^{-1}$ in the NH, and 228 and 265 nmol mol$^{-1}$ in the SH. In addition, Fig. 7 shows some relevant features related to ozone exchange in the UTLS. In the NH, we observe two regions where the ozone was relatively higher due to lower stratospheric ozone depletion: eastern North America (60° W) and Northeast Asia (140° E). In the SH, under low stratospheric ozone depletion, we observe a large region with relatively
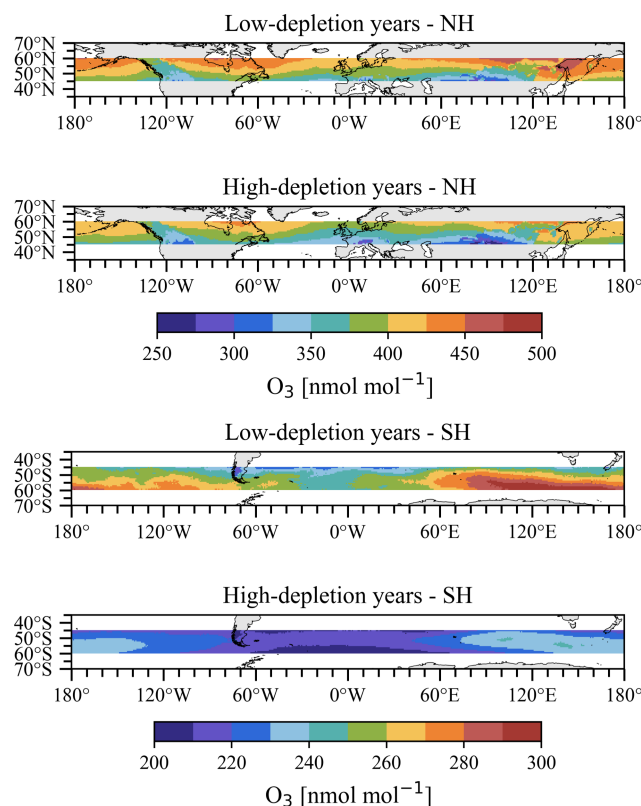


**Figure 7.** Ozone medians (nmol mol$^{-1}$) obtained from CAMS reanalysis filtered by RH less than 20 % at a resolution of $0.75° \times 0.75°$ and between 300–200 hPa. The upper panel depicts the ozone median in UTLS of the Northern Hemisphere, separated into low and high depletion years (entire period), while the lower panel describes the same for the Southern Hemisphere. Note that the color scales are different in the NH and SH given the strong differences in ozone mixing ratios.

higher ozone levels over the southern Indian Ocean and, to a minor degree, the South Pacific Ocean.

## 5 Conclusions

The SouthTRAC mission represents an invaluable contribution to atmospheric chemistry research in the Southern Hemisphere. This aircraft campaign provided unique data recorded during a rare stratospheric sudden warming event in the SH that caused profound effects on the chemical structure of the atmosphere, leveraged in this research as a proxy for a diminished ozone depletion scenario. The main conclusions of our research are listed below.

Tracer-to-tracer scatterplots between stratospheric ozone and tropospheric tracers (carbon monoxide and water vapor) are consistent with previous airborne campaign studies, which show high ozone and low carbon monoxide levels in the SH in both the free troposphere and the UTLS, which in this case was influenced by distant wildfires in Australia.

The bidirectional exchange observed in the UTLS during the 12 November 2019 flight provides evidence that transport from tropospheric sources can also influence this region of the atmosphere. During this flight, low levels of nitric acid ($<500$ pmol mol$^{-1}$) and hydrogen chloride ($<50$ pmol mol$^{-1}$) were consistently measured, alongside higher levels of carbon monoxide ($>200$ nmol mol$^{-1}$) and elevated water vapor ($>100$ µmol mol$^{-1}$), indicating a strong tropospheric signature in the UTLS.

The comparative analysis of ozone mixing ratios, with stratospheric origin between 300–200 hPa and 45–60° latitude, shows the following points.

i. Lower ozone levels in the SH UTLS compared with the NH. In high ozone depletion years, defined by the strength of the stratospheric vortex, the ozone median in the SH UTLS was 54 % of that in the NH UTLS. During years impacted by early SSW, i.e., low ozone depletion years, the SH UTLS ozone median was 57 % of the NH UTLS values.

ii. The difference between high and low ozone depletion years in the NH UTLS (March–May) as a function of SSW events resulted in a 9 % ozone enhancement ($31 \pm 11$ nmol mol$^{-1}$) compared with years without SSW. This enhancement was larger in the SH, reaching 24 % ($43 \pm 13$ nmol mol$^{-1}$).

iii. The chemical reanalysis is especially useful in areas with sparse in situ observations, such as the SH, and its application in this research allows us to assess the representativeness of in situ observations. Moreover, CAMSRA reproduced the ozone interhemispheric differences and the difference between high and low ozone depletion years in each hemisphere. Additionally, the CAMSRA-based analysis identified the southern Indian Ocean as the region with higher ozone in the UTLS.

Finally, differences in spatial coverage between the in situ measurements in the two hemispheres may affect the representativeness of the results and should be considered when interpreting these comparisons. Overall, this study emphasizes the need to expand highly resolved ozone profiles in the upper troposphere and lower stratosphere, particularly across the SH, where these measurements are crucial for accurately quantifying current STE processes and their impact on the tropospheric ozone budget.

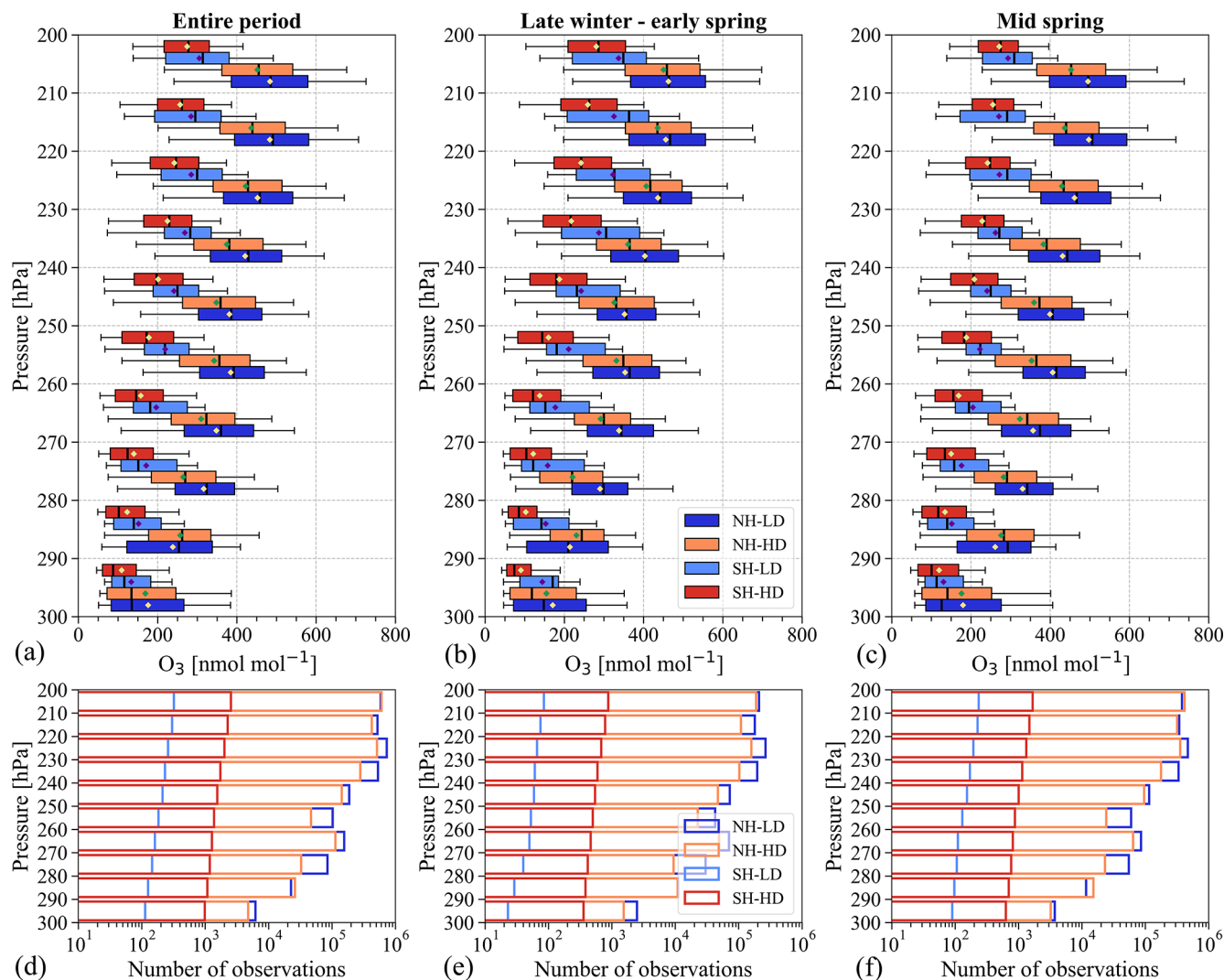## Appendix A: Ozone boxplot without RH filter
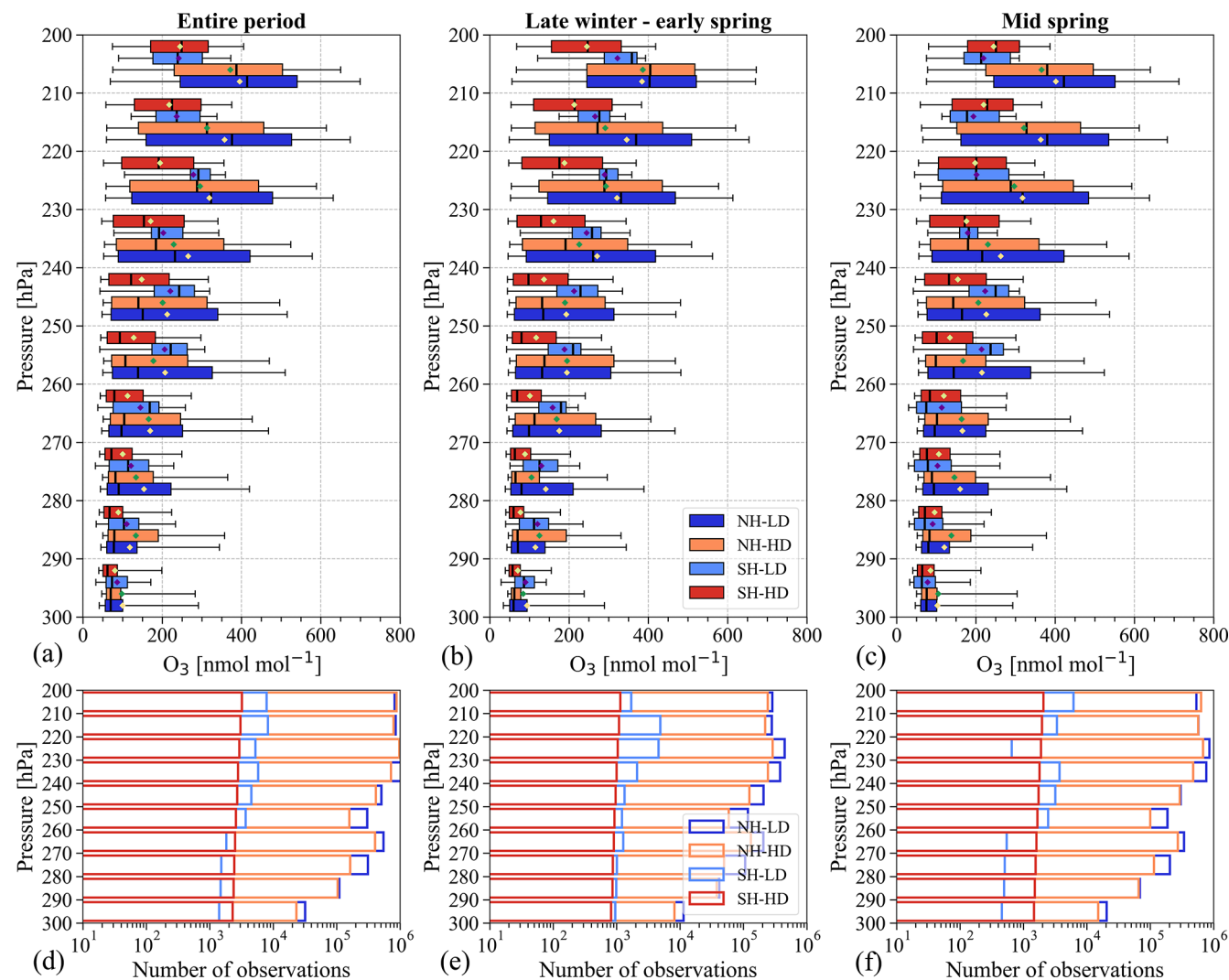


**Figure A1.** Ozone boxplot (nmol mol$^{-1}$) and associated sample sizes by pressure bins. The plots include ozone data, without RH filter, obtained from IAGOS, SouthTRAC and WOUDC (Table 1). In the upper panel, **(a)**, **(b)** and **(c)** show the entire period, late winter–early spring and mid-spring, respectively, for the Northern Hemisphere and Southern Hemisphere and HD and LD years. Boxplots indicate the median and the 25th and 75th percentiles. The diamonds in panels **(a)**–**(c)** indicate the mean values. The whiskers extend to the 5th and 95th percentiles. In **(d)**–**(f)**, the $x$ axis shows the observation numbers. The rest of the plot information is the same as described in panels **(a)**–**(c)**. High- and low-depletion years in SH included ozonesondes launched from Ushuaia, Lauder and Macquarie Island.

## Appendix B: Ozone boxplot without SouthTRAC data



**Figure B1.** Ozone boxplot (nmol mol$^{-1}$) and associated sample sizes by pressure bins. The plots include ozone data with RH less than 20 % obtained exclusively from IAGOS and WOUDC (Table 1). In the upper panel, **(a)**, **(b)** and **(c)** show the entire period, late winter–early spring and mid-spring, respectively, for the Northern Hemisphere and Southern Hemisphere and HD and LD years. Boxplots indicate the median and the 25th and 75th percentiles. The diamonds in panels **(a)**–**(c)** indicate the mean values. The whiskers extend to the 5th and 95th percentiles. In panels **(d)**–**(f)**, the $x$ axis shows the observation numbers. The rest of the plot information is the same as described in panels **(a)**–**(c)**. High- and low-depletion years in SH included ozonesondes launched from Ushuaia, Lauder and Macquarie Island.

## Appendix C:  Air masses filtered by carbon monoxide
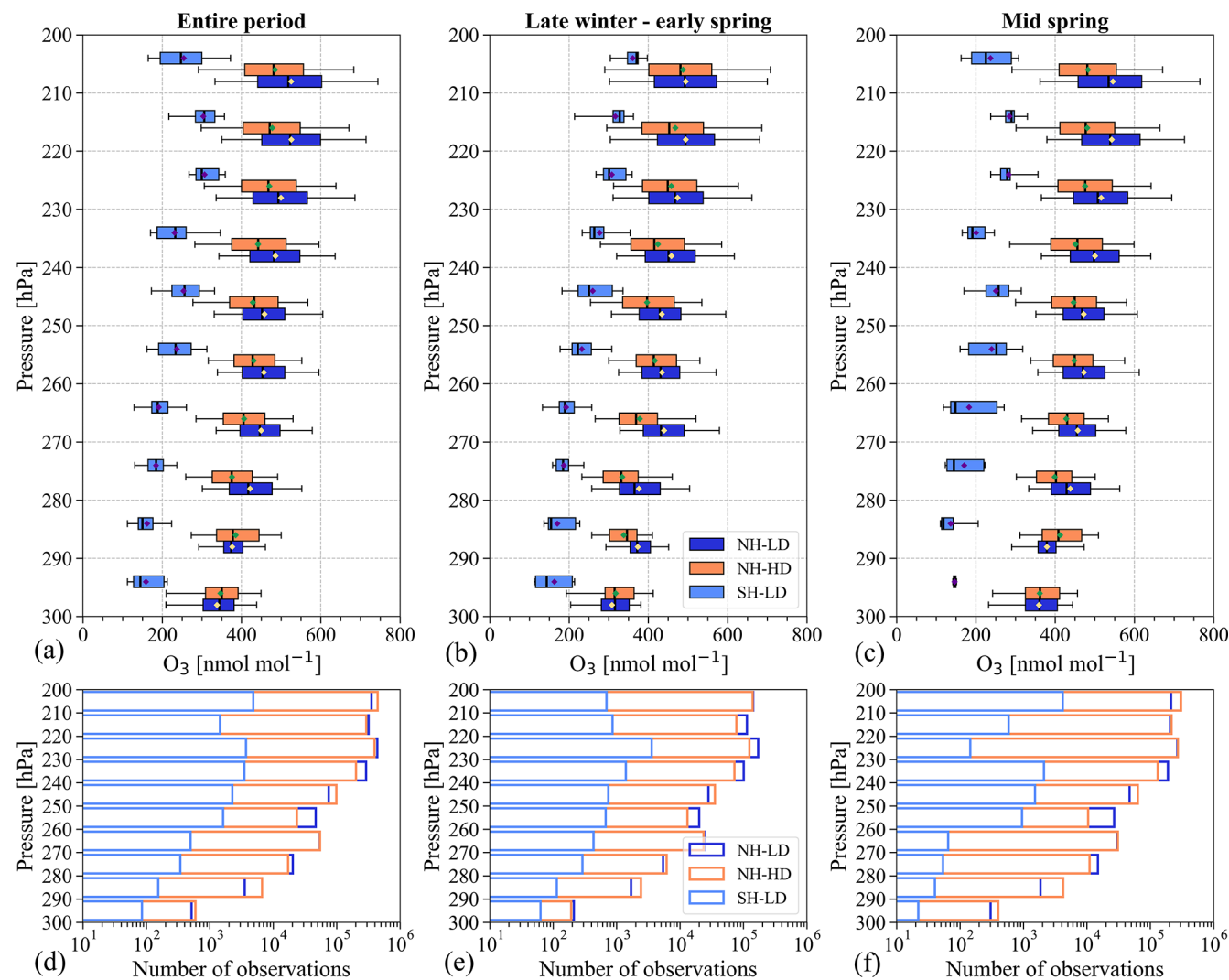


**Figure C1.** Ozone boxplot (nmol mol$^{-1}$) and associated observation numbers by pressure bins. The plots include ozone data with CO less than 50 nmol mol$^{-1}$. In the upper panel, **(a)**, **(b)** and **(c)** show the entire period, late winter–early spring and mid-spring for the Northern Hemisphere and Southern Hemisphere and HD and LD years. Boxplots indicate the median and the 25th and 75th percentiles. The diamonds in **(a)**–**(c)** indicate the mean values. The whiskers extend to the 5th and 95th percentiles. In panels **(d)**–**(f)**, the $x$ axis shows the observation numbers. The rest of the plot information is the same as described in **(a)**–**(c)**.

## References

Archibald, A. T., Neu, J. L., Elshorbany, Y. F., Cooper, O. R., Young, P. J., Akiyoshi, H., Cox, R. A., Coyle, M., Derwent, R. G., Deushi, M., Finco, A., Frost, G. J., Galbally, I. E., Gerosa, G., Granier, C., Griffiths, P. T., Hossaini, R., Hu, L., Jöckel, P., Josse, B., Lin, M. Y., Mertens, M., Morgenstern, O., Naja, M., Naik, V., Oltmans, S., Plummer, D. A., Revell, L. E., Saiz-Lopez, A., Saxena, P., Shin, Y. M., Shahid, I., Shallcross, D., Tilmes, S., Trickl, T., Wallington, T. J., Wang, T., Worden, H. M., and Zeng, G.: Tropospheric ozone assessment report: A critical review of changes in the tropospheric ozone burden and budget from 1850 to 2100, Elem. Sci. Anth., 8, 034, https://doi.org/10.1525/elementa.2020.034, 2020.

Atkinson, R.: Atmospheric chemistry of VOCs and NO$_x$, Atmos. Environ., 34, 2063–2101, https://doi.org/10.1016/S1352-2310(99)00460-4, 2000.

Bourgeois, I., Peischl, J., Thompson, C. R., Aikin, K. C., Campos, T., Clark, H., Commane, R., Daube, B., Diskin, G. W., Elkins, J. W., Gao, R.-S., Gaudel, A., Hintsa, E. J., Johnson, B. J., Kivi, R., McKain, K., Moore, F. L., Parrish, D. D., Querel, R., Ray, E., Sánchez, R., Sweeney, C., Tarasick, D. W., Thompson, A. M., Thouret, V., Witte, J. C., Wofsy, S. C., and Ryerson, T. B.: Global-scale distribution of ozone in the remote troposphere from the ATom and HIPPO airborne field missions, Atmos. Chem. Phys., 20, 10611–10635, https://doi.org/10.5194/acp-20-10611-2020, 2020.

Brenninkmeijer, C. A. M., Crutzen, P. J., Fischer, H., Güsten, H., Hans, W., Heinrich, G., Heintzenberg, J., Hermann, M.,

Immelmann, T., Kersting, D., Maiss, M., Nolle, M., Pitscheider, A., Pohlkamp, H., Scharffe, D., Specht, K., and Wiedensohler, A.: CARIBIC-Civil Aircraft for global measurement of trace gases and aerosols in the tropopause region, J. Atmos. Ocean. Tech., 16, 1373–1383, https://doi.org/10.1175/1520-0426(1999)016<1373:CCAFGM>2.0.CO;2, 1999.

Brenninkmeijer, C. A. M., Crutzen, P., Boumard, F., Dauer, T., Dix, B., Ebinghaus, R., Filippi, D., Fischer, H., Franke, H., Frieβ, U., Heintzenberg, J., Helleis, F., Hermann, M., Kock, H. H., Koeppel, C., Lelieveld, J., Leuenberger, M., Martinsson, B. G., Miemczyk, S., Moret, H. P., Nguyen, H. N., Nyfeler, P., Oram, D., O'Sullivan, D., Penkett, S., Platt, U., Pupek, M., Ramonet, M., Randa, B., Reichelt, M., Rhee, T. S., Rohwer, J., Rosenfeld, K., Scharffe, D., Schlager, H., Schumann, U., Slemr, F., Sprung, D., Stock, P., Thaler, R., Valentino, F., van Velthoven, P., Waibel, A., Wandel, A., Waschitschek, K., Wiedensohler, A., Xueref-Remy, I., Zahn, A., Zech, U., and Ziereis, H.: Civil Aircraft for the regular investigation of the atmosphere based on an instrumented container: The new CARIBIC system, Atmos. Chem. Phys., 7, 4953–4976, https://doi.org/10.5194/acp-7-4953-2007, 2007.

Butchart, N.: The Brewer-Dobson circulation, Rev. Geophys., 52, 157–184, https://doi.org/10.1002/2013RG000448, 2014.

Charlton, A. J. and Polvani, L. M.: A new look at stratospheric sudden warmings. Part I: Climatology and modeling benchmarks, J. Climate, 20, 449–469, https://doi.org/10.1175/JCLI3996.1, 2007.

Clifton, O. E., Fiore, A. M., Massman, W. J., Baublitz, C. B., Coyle, M., Emberson, L., Fares, S., Farmer, D. K., Gentine, P., Gerosa, G., Guenther, A. B., Helmig, D., Lombardozzi, D. L., Munger, J. W., Patton, E. G., Pusede, S. E., Schwede, D. B., Silva, S. J., Sörgel, M., Steiner, A. L., and Tai, A. P. K.: Dry Deposition of Ozone Over Land: Processes, Measurement, and Modeling, Rev. Geophys., 58, e2019RG00067, https://doi.org/10.1029/2019RG000670, 2020.

Cooper, O., Forster, C., Parrish, D., Dunlea, E., Hübler, G., Fehsenfeld, F., Holloway, J., Oltmans, S., Johnson, B., Wimmers, A., and Horowitz, L.: On the life cycle of a stratospheric intrusion and its dispersion into polluted warm conveyor belts, J. Geophys. Res.-Atmos., 109, D23S09, https://doi.org/10.1029/2003JD004006, 2004.

Copernicus Atmosphere Monitoring Service: CAMS global reanalysis (EAC4), Copernicus Atmosphere Monitoring Service (CAMS) Atmosphere Data Store [data set], https://doi.org/10.24381/d58bbf47, 2020.

Dunn, R. J. H., Stanitski, D. M., Gobron, N., and Willett, K. M. (Eds.): Global Climate, in: State of the Climate in 2019, B. Am. Meteorol. Soc., 101, S9–S127, https://doi.org/10.1175/BAMS-D-20-0104.1, 2020.

Dyroff, C., Zahn, A., Christner, E., Forbes, R., Tompkins, A. M., and van Velthoven, P. F. J.: Comparison of ECMWF analysis and forecast humidity data with CARIBIC upper troposphere and lower stratosphere observations, Q. J. Roy. Meteor. Soc., 141, 833–844, https://doi.org/10.1002/qj.2400, 2015.

Ermel, M., Oswald, R., Mayer, J. C., Moravek, A., Song, G., Beck, M., Meixner, F. X., and Trebs, I.: Preparation methods to optimize the performance of sensor discs for fast chemiluminescence ozone analyzers, Environ. Sci. Technol., 47, 1930–1936, https://doi.org/10.1021/es3040363, 2013.

Forster, P., Storelvmo, T., Armour, K.,x Collins, K., Dufresne, J.-L., Frame, D., Lunt, D. J., Mauritsen, T., Palmer, M. D., Watanabe, M., Wild, M., and Zhang, H.: The Earth's Energy Budget, Climate Feedbacks, and Climate Sensitivity, in: Climate Change 2021: The Physical Science Basis. Contribution of Working Group I to the Sixth Assessment Report of the Intergovernmental Panel on Climate Change, edited by: Masson-Delmotte, V., Zhai, P., Pirani, A., Connors, S. L., Péan, C., Berger, S., Caud, N., Chen, Y., Goldfarb, L., Gomis, M. I., Huang, M., Leitzell, K., Lonnoy, E., Matthews, J. B. R., Maycock, T. K., Waterfield, T., Yelekçi, O., Yu, R., and Zhou, B., Cambridge University Press, Cambridge, United Kingdom and New York, NY, USA, 923–1054, https://doi.org/10.1017/9781009157896.009, 2021.

Garfinkel, C. I., Aquila, V., Waugh, D. W., and Oman, L. D.: Time-varying changes in the simulated structure of the Brewer–Dobson Circulation, Atmos. Chem. Phys., 17, 1313–1327, https://doi.org/10.5194/acp-17-1313-2017, 2017.

Gettelman, a., Pan, L. L., Randel, W. J., Hoor, P., Birner, T., and Hegglin, M. I.: the Extratropical Upper Troposphere and Lower Stratosphere, Rev. Geophys., 49, RG3003, https://doi.org/10.1029/2011RG000355, 2011.

Giez, A., Mallaun, C., Zöger, M., Dörnbrack, A., and Schumann, U.: Static pressure from aircraft trailing-cone measurements and numerical weather-prediction analysis, J. Aircraft, 54, 5, https://doi.org/10.2514/1.C034084, 2017.

Griffiths, P. T., Murray, L. T., Zeng, G., Shin, Y. M., Abraham, N. L., Archibald, A. T., Deushi, M., Emmons, L. K., Galbally, I. E., Hassler, B., Horowitz, L. W., Keeble, J., Liu, J., Moeini, O., Naik, V., O'Connor, F. M., Oshima, N., Tarasick, D., Tilmes, S., Turnock, S. T., Wild, O., Young, P. J., and Zanis, P.: Tropospheric ozone in CMIP6 simulations, Atmos. Chem. Phys., 21, 4187–4218, https://doi.org/10.5194/acp-21-4187-2021, 2021.

HALO Database: SouthTRAC mission, HALO Database [data set], https://halo-db.pa.op.dlr.de/mission/116, last access: 31 July 2024.

Health Effects Institute: State of Global Air 2020, Special Report, Health Effects Instiute, https://www.stateofglobalair.org/resources/archived/state-global-air-report-2020 (last access: 1 November 2024), 2020.

Helten, M., Smit, H. G. J., Sträter, W., Kley, D., Nedelec, P., Zöger, M., and Busen, R.: Calibration and performance of automatic compact instrumentation for the measurement of relative humidity from passenger aircraft, J. Geophys. Res.-Atmos., 103, 25643–25652, https://doi.org/10.1029/98JD00536, 1998.

Hersbach, H., Comyn-Platt, E., Bell, B., Berrisford, P., Biavati, G., Horányi, A., Muñoz Sabater, J., Nicolas, J., Peubey, C., Radu, R., Rozum, I., Schepers, D., Simmons, A., Soci, C., Dee, D., Thépaut, J-N., Cagnazzo, C., and Cucchi, M.: ERA5 post-processed daily-statistics on pressure levels from 1940 to present, Copernicus Climate Change Service (C3S) Climate Data Store (CDS) [data set], https://doi.org/10.24381/cds.50314f4c, 2023.

Inness, A., Ades, M., Agustí-Panareda, A., Barré, J., Benedictow, A., Blechschmidt, A.-M., Dominguez, J. J., Engelen, R., Eskes, H., Flemming, J., Huijnen, V., Jones, L., Kipling, Z., Massart, S., Parrington, M., Peuch, V.-H., Razinger, M., Remy, S., Schulz, M., and Suttie, M.: The CAMS reanalysis of atmospheric composition, Atmos. Chem. Phys., 19, 3515–3556, https://doi.org/10.5194/acp-19-3515-2019, 2019.

Jensen, M. P., Holdridge, D. J., Survo, P., Lehtinen, R., Baxter, S., Toto, T., and Johnson, K. L.: Comparison of Vaisala radiosondes RS41 and RS92 at the ARM Southern Great Plains site, Atmos. Meas. Tech., 9, 3115–3129, https://doi.org/10.5194/amt-9-3115-2016, 2016.

Johansson, S., Wetzel, G., Friedl-Vallon, F., Glatthor, N., Höpfner, M., Kleinert, A., Neubert, T., Sinnhuber, B.-M., and Ungermann, J.: Biomass burning pollution in the South Atlantic upper troposphere: GLORIA trace gas observations and evaluation of the CAMS model, Atmos. Chem. Phys., 22, 3675–3691, https://doi.org/10.5194/acp-22-3675-2022, 2022.

Jurkat, T., Kaufmann, S., Voigt, C., Schäuble, D., Jeßberger, P., and Ziereis, H.: The airborne mass spectrometer AIMS – Part 2: Measurements of trace gases with stratospheric or tropospheric origin in the UTLS, Atmos. Meas. Tech., 9, 1907–1923, https://doi.org/10.5194/amt-9-1907-2016, 2016.

Kaufmann, S., Voigt, C., Heller, R., Jurkat-Witschas, T., Krämer, M., Rolf, C., Zöger, M., Giez, A., Buchholz, B., Ebert, V., Thornberry, T., and Schumann, U.: Intercomparison of midlatitude tropospheric and lower-stratospheric water vapor measurements and comparison to ECMWF humidity data, Atmos. Chem. Phys., 18, 16729–16745, https://doi.org/10.5194/acp-18-16729-2018, 2018.

Kloss, C., Sellitto, P., von Hobe, M., Berthet, G., Smale, D., Krysztofiak, G., Xue, C., Qiu, C., Jégou, F., Ouerghemmi, I., and Legras, B.: Australian Fires 2019–2020: Tropospheric and Stratospheric Pollution Throughout the Whole Fire Season, Front. Environ. Sci., 9, 652024, https://doi.org/10.3389/fenvs.2021.652024, 2021.

Lim, E. P., Hendon, H. H., Butler, A. H., Thompson, D. W. J., Lawrence, Z. D., Scaife, A. A., Shepherd, T. G., Polichtchouk, I., Nakamura, H., Kobayashi, C., Comer, R., Coy, L., Dowdy, A., Garreaud, R. D., Newman, P. A., and Wang, G.: The 2019 southern hemisphere stratospheric polar vortex weakening and its impacts, B. Am. Meteorol. Soc., 102, https://doi.org/10.1175/BAMS-D-20-0112.1, 2021.

Lu, X., Zhang, L., Zhao, Y., Jacob, D. J., Hu, Y., Hu, L., Gao, M., Liu, X., Petropavlovskikh, I., McClure-Begley, A., and Querel, R.: Surface and tropospheric ozone trends in the Southern Hemisphere since 1990: possible linkages to poleward expansion of the Hadley circulation, Sci. Bull. (Beijing), 64, 400–409, https://doi.org/10.1016/j.scib.2018.12.021, 2019.

Marenco, A., Thouret, V., Nédélec, P., Smit, H., Helten, M., Kley, D., Karcher, F., Simon, P., Law, K., Pyle, J., Poschmann, G., Von Wrede, R., Hume, C., and Cook, T.: Measurement of ozone and water vapor by Airbus in-service aircraft: The MOZAIC airborne program, An overview, J. Geophys. Res.-Atmos., 103, 25631–25642, https://doi.org/10.1029/98JD00977, 1998.

McConnell, R., Berhane, K., Gilliland, F., London, S. J., Islam, T., Gauderman, W. J., Avol, E., Margolis, H. G., and Peters, J. M.: Asthma in exercising children exposed to ozone: A cohort study, Lancet, 359, 286–391, https://doi.org/10.1016/S0140-6736(02)07597-9, 2002.

Millán, L. F., Hoor, P., Hegglin, M. I., Manney, G. L., Boenisch, H., Jeffery, P., Kunkel, D., Petropavlovskikh, I., Ye, H., Leblanc, T., and Walker, K.: Exploring ozone variability in the upper troposphere and lower stratosphere using dynamical coordinates, Atmos. Chem. Phys., 24, 7927–7959, https://doi.org/10.5194/acp-24-7927-2024, 2024.

Monks, P. S., Archibald, A. T., Colette, A., Cooper, O., Coyle, M., Derwent, R., Fowler, D., Granier, C., Law, K. S., Mills, G. E., Stevenson, D. S., Tarasova, O., Thouret, V., von Schneidemesser, E., Sommariva, R., Wild, O., and Williams, M. L.: Tropospheric ozone and its precursors from the urban to the global scale from air quality to short-lived climate forcer, Atmos. Chem. Phys., 15, 8889–8973, https://doi.org/10.5194/acp-15-8889-2015, 2015.

Müller, S., Hoor, P., Berkes, F., Bozem, H., Klingebiel, M., Reutter, P., Smit, H. G. J., Wendisch, M., Spichtinger, P., and Borrmann, S.: In situ detection of stratosphere-troposphere exchange of cirrus particles in the midlatitudes, Geophys. Res. Lett., 42, 949–955, https://doi.org/10.1002/2014GL062556, 2015.

Nedelec, P., Cammas, J.-P., Thouret, V., Athier, G., Cousin, J.-M., Legrand, C., Abonnel, C., Lecoeur, F., Cayez, G., and Marizy, C.: An improved infrared carbon monoxide analyser for routine measurements aboard commercial Airbus aircraft: technical validation and first scientific results of the MOZAIC III programme, Atmos. Chem. Phys., 3, 1551–1564, https://doi.org/10.5194/acp-3-1551-2003, 2003.

Nédélec, P., Blot, R., Boulanger, D., Athier, G., Cousin, J. M., Gautron, B., Petzold, A., Volz-Thomas, A., and Thouret, V.: Instrumentation on commercial aircraft for monitoring the atmospheric composition on a global scale: The IAGOS system, technical overview of ozone and carbon monoxide measurements, Tellus B, 67, 27791, https://doi.org/10.3402/tellusb.v67.27791, 2015.

Neis, P., Smit, H. G. J., Rohs, S., Bundke, U., Krämer, M., Spelten, N., Ebert, V., Buchholz, B., Thomas, K., and Petzold, A.: Quality assessment of MOZAIC and IAGOS capacitive hygrometers: Insights from airborne field studies, Tellus B, 67, 28320, https://doi.org/10.3402/tellusb.v67.28320, 2015.

Neu, J. L., Hegglin, M. I., Tegtmeier, S., Bourassa, A., Degenstein, D., Froidevaux, L., Fuller, R., Funke, B., Gille, J., Jones, A., Rozanov, A., Toohey, M., Von Clarmann, T., Walker, K. A., and Worden, J. R.: The SPARC data initiative: Comparison of upper troposphere/lower stratosphere ozone climatologies from limb-viewing instruments and the nadir-viewing tropospheric emission spectrometer, J. Geophys. Res., 119, 11, 6971–6990, https://doi.org/10.1002/2013JD020822, 2014.

Ohyama, H., Mizuno, A., Zamorano, F., Sugita, T., Akiyoshi, H., Noguchi, K., Wolfram, E., Salvador, J., and Benitez, G. C.: Characteristics of Atmospheric Wave-Induced Laminae Observed by Ozonesondes at the Southern Tip of South America, J. Geophys. Res.-Atmos., 123, 11811–11829, https://doi.org/10.1029/2018JD028707, 2018.

Petzold, A., Thouret, V., Gerbig, C., Zahn, A., Brenninkmeijer, C. A. M., Gallagher, M., Hermann, M., Pontaud, M., Ziereis, H., Boulanger, D., Marshall, J., NéDélec, P., Smit, H. G. J., Friess, U., Flaud, J. M., Wahner, A., Cammas, J. P., Volz-Thomas, A., Thomas, K., Rohs, S., Bundke, U., Neis, P., Berkes, F., Houben, N., Berg, M., Tappertzhofen, M., Blomel, T., Pätz, W., Filges, A., Boschetti, F., Verma, S., Baum, S., Athier, G., Cousin, J. M., Sauvage, B., Blot, R., Clark, H., Gaudel, A., Gressent, A., Auby, A., Fontaine, A., Gautron, B., Bennouna, Y., Petetin, H., Karcher, F., Abonnel, C., Dandin, P., Beswick, K., Wang, K. Y., Rauthe-Schöch, A., Baker, A. K., Riede, H., Gromov, S., Zimmermann, P., Thorenz, U., Scharffe, D., Koeppel, C., Slemr, F., Schuck, T. J., Umezawa, T., Ditas, J., Cheng, Y., Schneider, J., Williams, J., Neumaier, M., Christner, E., Fischbeck, G., Safadi, L., Petrelli,

A., Gehrlein, T., Heger, S., Dyroff, C., Weber, S., Assmann, D., Rubach, F., Weigelt, A., Stratmann, G., Stock, P., Penth, L., Walter, D., Heue, K. P., Allouche, Y., Marizy, C., Hermira, J., Bringtown, S., Saueressig, G., Seidel, N., Huf, M., Waibel, A., Franke, H., Klaus, C., Stosius, R., Baumgardner, D., Braathen, G., Paulin, M., and Garnett, N.: Global-scale atmosphere monitoring by in-service aircraft – current achievements and future prospects of the European Research Infrastructure IAGOS, Tellus B, 67, 28452, https://doi.org/10.3402/tellusb.v67.28452, 2015.

Rao, J., Garfinkel, C. I., White, I. P., and Schwartz, C.: The Southern Hemisphere Minor Sudden Stratospheric Warming in September 2019 and its Predictions in S2S Models, J. Geophys. Res.-Atmos., 125, e2020JD032723, https://doi.org/10.1029/2020JD032723, 2020.

Rapp, M., Kaifler, B., Dörnbrack, A., Gisinger, S., Mixa, T., Reichert, R., Kaifler, N., Knobloch, S., Eckert, R., Wildmann, N., Giez, A., Krasauskas, L., Preusse, P., Geldenhuys, M., Riese, M., Woiwode, W., Friedl-Vallon, F., Sinnhuber, B. M., De la Torre, A., Alexander, P., Hormaechea, J. L., Janches, D., Garhammer, M., Chau, J. L., Federico Conte, J., Hoor, P., and Engel, A.: Southtrac-gw: An airborne field campaign to explore gravity wave dynamics at the world's strongest hotspot, B. Am. Meteorol. Soc., 102, E871–E893, https://doi.org/10.1175/BAMS-D-20-0034.1, 2021.

Riese, M., Ploeger, F., Rap, A., Vogel, B., Konopka, P., Dameris, M., and Forster, P.: Impact of uncertainties in atmospheric mixing on simulated UTLS composition and related radiative effects, J. Geophys. Res.-Atmos., 117, D16305, https://doi.org/10.1029/2012JD017751, 2012.

Rolf, C., Afchine, A., Bozem, H., Buchholz, B., Ebert, V., Guggenmoser, T., Hoor, P., Konopka, P., Kretschmer, E., Müller, S., Schlager, H., Spelten, N., Sumińska-Ebersoldt, O., Ungermann, J., Zahn, A., and Krämer, M.: Transport of Antarctic stratospheric strongly dehydrated air into the troposphere observed during the HALO-ESMVal campaign 2012, Atmos. Chem. Phys., 15, 9143–9158, https://doi.org/10.5194/acp-15-9143-2015, 2015.

Rolf, C., Rohs, S., Smit, H. G. J., Krämer, M., Bozóki, Z., Hofmann, S., Franke, H., Maser, R., Hoor, P., and Petzold, A.: Evaluation of compact hygrometers for continuous airborne measurements, Meteorol. Z., 33, 15–34, https://doi.org/10.1127/metz/2023/1187, 2024.

Saunois, M., Stavert, A. R., Poulter, B., Bousquet, P., Canadell, J. G., Jackson, R. B., Raymond, P. A., Dlugokencky, E. J., Houweling, S., Patra, P. K., Ciais, P., Arora, V. K., Bastviken, D., Bergamaschi, P., Blake, D. R., Brailsford, G., Bruhwiler, L., Carlson, K. M., Carrol, M., Castaldi, S., Chandra, N., Crevoisier, C., Crill, P. M., Covey, K., Curry, C. L., Etiope, G., Frankenberg, C., Gedney, N., Hegglin, M. I., Höglund-Isaksson, L., Hugelius, G., Ishizawa, M., Ito, A., Janssens-Maenhout, G., Jensen, K. M., Joos, F., Kleinen, T., Krummel, P. B., Langenfelds, R. L., Laruelle, G. G., Liu, L., Machida, T., Maksyutov, S., McDonald, K. C., McNorton, J., Miller, P. A., Melton, J. R., Morino, I., Müller, J., Murguia-Flores, F., Naik, V., Niwa, Y., Noce, S., O'Doherty, S., Parker, R. J., Peng, C., Peng, S., Peters, G. P., Prigent, C., Prinn, R., Ramonet, M., Regnier, P., Riley, W. J., Rosentreter, J. A., Segers, A., Simpson, I. J., Shi, H., Smith, S. J., Steele, L. P., Thornton, B. F., Tian, H., Tohjima, Y., Tubiello, F. N., Tsuruta, A., Viovy, N., Voulgarakis, A., Weber, T. S.,

van Weele, M., van der Werf, G. R., Weiss, R. F., Worthy, D., Wunch, D., Yin, Y., Yoshida, Y., Zhang, W., Zhang, Z., Zhao, Y., Zheng, B., Zhu, Q., Zhu, Q., and Zhuang, Q.: The Global Methane Budget 2000–2017, Earth Syst. Sci. Data, 12, 1561–1623, https://doi.org/10.5194/essd-12-1561-2020, 2020.

Scambos, T. and Stammerjohn, and S. (Eds.): Antactica and the Southern Ocean, B. Am. Meteorol. Soc., 101, S287–S320, https://doi.org/10.1175/BAMS-D-20-0090.1, 2020.

Scharffe, D., Slemr, F., Brenninkmeijer, C. A. M., and Zahn, A.: Carbon monoxide measurements onboard the CARIBIC passenger aircraft using UV resonance fluorescence, Atmos. Meas. Tech., 5, 1753–1760, https://doi.org/10.5194/amt-5-1753-2012, 2012.

Skeie, R. B., Myhre, G., Hodnebrog, Ø., Cameron-Smith, P. J., Deushi, M., Hegglin, M. I., Horowitz, L. W., Kramer, R. J., Michou, M., Mills, M. J., Olivié, D. J. L., Connor, F. M. O., Paynter, D., Samset, B. H., Sellar, A., Shindell, D., Takemura, T., Tilmes, S., and Wu, T.: Historical total ozone radiative forcing derived from CMIP6 simulations, NPJ. Clim. Atmos. Sci., 3, 32, https://doi.org/10.1038/s41612-020-00131-0, 2020.

Škerlak, B., Sprenger, M., and Wernli, H.: A global climatology of stratosphere–troposphere exchange using the ERA-Interim data set from 1979 to 2011, Atmos. Chem. Phys., 14, 913–937, https://doi.org/10.5194/acp-14-913-2014, 2014.

Smit, H. G. J., Rohs, S., Neis, P., Boulanger, D., Krämer, M., Wahner, A., and Petzold, A.: Technical Note: Reanalysis of upper troposphere humidity data from the MOZAIC programme for the period 1994 to 2009, Atmos. Chem. Phys., 14, 13241–13255, https://doi.org/10.5194/acp-14-13241-2014, 2014.

Stohl, A., Bonasoni, P., Cristofanelli, P., Collins, W., Feichter, J., Frank, A., Forster, C., Gerasopoulos, E., Gäggeler, H., James, P., Kentarchos, T., Kromp-Kolb, H., Krüger, B., Land, C., Meloen, J., Papayannis, A., Priller, A., Seibert, P., Sprenger, M., Roelofs, G. J., Scheel, H. E., Schnabel, C., Siegmund, P., Tobler, L., Trickl, T., Wernli, H., Wirth, V., Zanis, P., and Zerefos, C.: Stratosphere-troposphere exchange: A review, and what we have learned from STACCATO, J. Geophys. Res.-Atmos., 108, 8516, https://doi.org/10.1029/2002jd002490, 2003.

Stratmann, G., Ziereis, H., Stock, P., Brenninkmeijer, C. A. M., Zahn, A., Rauthe-Schöch, A., Velthoven, P. V., Schlager, H., and Volz-Thomas, A.: NO and NO$_y$ in the upper troposphere: Nine years of CARIBIC measurements onboard a passenger aircraft, Atmos. Environ., 133, 93–111, https://doi.org/10.1016/j.atmosenv.2016.02.035, 2016.

Szopa, S., Naik, V., Adhikary, B., Artaxo, P., Berntsen, T., Collins, W.D., Fuzzi, S., Gallardo, L., Kiendler-Scharr, A., Klimont, Z., Liao, H., Unger, N., and Zanis, P.: Short-Lived Climate Forcers, in: Climate Change 2021: The Physical Science Basis. Contribution of Working Group I to the Sixth Assessment Report of the Intergovernmental Panel on Climate Change, edited by: Masson-Delmotte, V., Zhai, P., Pirani, A., Connors, S. L., Péan, C., Berger, S., Caud, N., Chen, Y., Goldfarb, L., Gomis, M. I., Huang, M., Leitzell, K., Lonnoy, E., Matthews, J. B. R., Maycock, T. K., Waterfield, T., Yelekçi, O., Yu, R., and Zhou, B., Cambridge University Press, Cambridge, United Kingdom and New York, NY, USA, 817–922, https://doi.org/10.1017/9781009157896.008, 2021

Thouret, V., Marenco, A., Logan, J. A., Nédélec, P., and Grouhel, C.: Comparisons of ozone measurements from the

MOZAIC airborne program and the ozone sounding network at eight locations, J. Geophys. Res.-Atmos., 103 25695–25720, https://doi.org/10.1029/98JD02243, 1998.

TOAR-II HEGIFTOM Focus Working Group: Harmonization and Evaluation of Ground-based Instruments for Free Tropospheric Ozone Measurements (HEGIFTOM), RMI [data set], https://hegiftom.meteo.be, last access: 11 February 2025.

Van Malderen, R., Thompson, A. M., Kollonige, D. E., Stauffer, R. M., Smit, H. G. J., Maillard Barras, E., Vigouroux, C., Petropavlovskikh, I., Leblanc, T., Thouret, V., Wolff, P., Effertz, P., Tarasick, D. W., Poyraz, D., Ancellet, G., De Backer, M.-R., Evan, S., Flood, V., Frey, M. M., Hannigan, J. W., Hernandez, J. L., Iarlori, M., Johnson, B. J., Jones, N., Kivi, R., Mahieu, E., McConville, G., Müller, K., Nagahama, T., Notholt, J., Piters, A., Prats, N., Querel, R., Smale, D., Steinbrecht, W., Strong, K., and Sussmann, R.: Global Ground-based Tropospheric Ozone Measurements: Reference Data and Individual Site Trends (2000–2022) from the TOAR-II/HEGIFTOM Project, EGUsphere [preprint], https://doi.org/10.5194/egusphere-2024-3736, 2025.

WOUDC: Index of /archive/Archive-NewFormat/OzoneSonde_1.0_1/stn339/ecc, WOUDC [data set], http://woudc.org/archive/Archive-NewFormat/OzoneSonde_1.0_1/stn339/ecc, last access: 31 July 2024.

Zahn, A., Weppner, J., Widmann, H., Schlote-Holubek, K., Burger, B., Kühner, T., and Franke, H.: A fast and precise chemiluminescence ozone detector for eddy flux and airborne application, Atmos. Meas. Tech., 5, 363–375, https://doi.org/10.5194/amt-5-363-2012, 2012.

Zahn, A., Christner, E., Van Velthoven, P. F. J., Rauthe-Schöch, A., and Brenninkmeijer, C. A. M.: Processes controlling water vapor in the upper troposphere/lowermost stratosphere: An analysis of 8years of monthly measurements by the IAGOS-CARIBIC observatory, J. Geophys. Res., 119, 11505–11525, https://doi.org/10.1002/2014JD021687, 2014.

Zahn, A., Obersteiner, F., Gehrlein, T., Neumaier, M., Dyroff, C., Förster, E., Sprung, D., Van Velthoven, P., Xueref-Remy, I., Ziereis, H., Bundke, U., Gerbig, C., Scharffe, D., Slemr, F., Weber, S., Hermann, M., Cheng, Y., and Bönisch, H.: IAGOS-CARIBIC MS files collection (v2024.10.28), Zenodo [data set], https://doi.org/10.5281/zenodo.8188548, 2024.

Zeng, G., Querel, R., Shiona, H., Poyraz, D., Van Malderen, R., Geddes, A., Smale, P., Smale, D., Robinson, J., and Morgenstern, O.: Analysis of a newly homogenised ozonesonde dataset from Lauder, New Zealand, Atmos. Chem. Phys., 24, 6413–6432, https://doi.org/10.5194/acp-24-6413-2024, 2024.

Zheng, X. yan, Orellano, P., Lin, H. liang, Jiang, M., and Guan, W. jie: Short-term exposure to ozone, nitrogen dioxide, and sulphur dioxide and emergency department visits and hospital admissions due to asthma: A systematic review and meta-analysis, Environ. Int., 150, 106435 https://doi.org/10.1016/j.envint.2021.106435, 2021.